7
Track detectors

Some scientists find, or so it seems, that they get their best ideas when smoking; others by drinking coffee or whiskey. Thus there is no reason why I should not admit that some may get their ideas by observing or by repeating observations.

Karl R. Popper

The measurement of particle trajectories is a very important issue for any experiment in high energy physics. This provides information about the interaction point, the decay path of unstable particles, angular distributions and, when the particle travels in a magnetic field, its momentum. Track detectors, used intensively in particle physics up to the early seventies, have been described in Chap. 6.

A new epoch was opened by the invention of the multiwire proportional chamber [1, 2]. Now gaseous wire chambers and micropattern detectors almost play a dominant rôle in the class of track detectors.

The fast progress of semiconductor detectors has resulted in a growth of the number of high energy physics experiments using tracking systems based on semiconductor microstrip or pixel detectors, especially in areas where extremely high spatial accuracy is required.

7.1 Multiwire proportional chambers

A *multiwire proportional chamber* (MWPC) [1–4] is essentially a planar layer of proportional counters without separating walls (Fig. 7.1). The shape of the electric field is somewhat modified compared to the pure cylindrical arrangement in proportional counters (Fig. 7.2) [5, 6].

https://doi.org/10.1017/9781009401531.010 Published online by Cambridge University Press

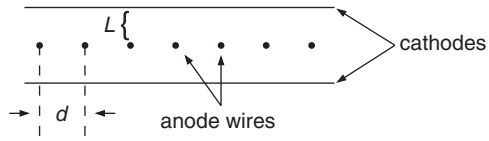

Fig. 7.1. Schematic layout of the construction of a multiwire proportional chamber.

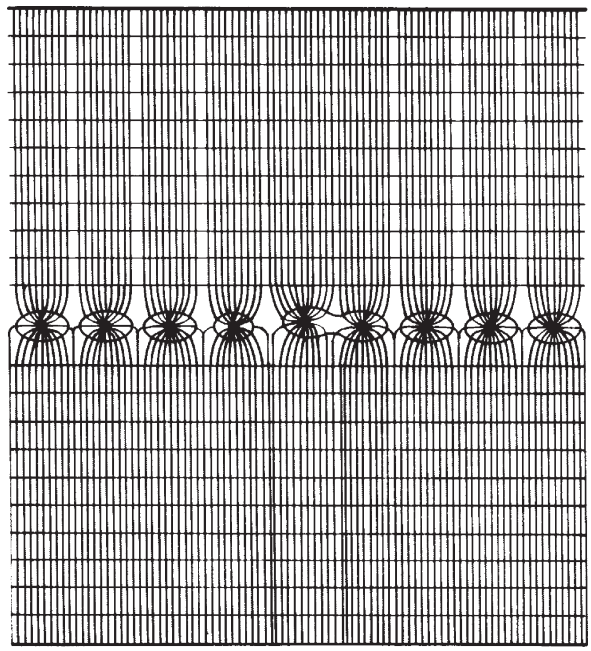

Fig. 7.2. Field and equipotential lines in a multiwire proportional chamber. The effect of a minor displacement of one anode wire on the field quality is clearly visible [5, 6].

When the coordinates of the wires are $y = 0, x = 0, \pm d, \pm 2d, \ldots$ the potential distribution is approximated by an analytical form [6]:

$$U(x,y) = \frac{CV}{4\pi\varepsilon_0}\left\{\frac{2\pi L}{d} - \ln\left[4\left(\sin^2\frac{\pi x}{d} + \sinh^2\frac{\pi y}{d}\right)\right]\right\} \ , \qquad (7.1)$$

where L and d are defined in Fig. 7.1, V is the anode voltage, ε_0 the permittivity of free space ($\varepsilon_0 = 8.854 \cdot 10^{-12}$ F/m), and C the capacitance per unit length given by the formula

$$C = \frac{4\pi\varepsilon_0}{2\left(\frac{\pi L}{d} - \ln\frac{2\pi r_\mathrm{i}}{d}\right)} \ , \qquad (7.2)$$

where r_i is the anode-wire radius.

https://doi.org/10.1017/9781009401531.010 Published online by Cambridge University Press

Avalanche formation in a multiwire proportional chamber proceeds exactly in the same way as in proportional counters. Since for each anode wire the bulk charge is produced in its immediate vicinity, the signal originates predominantly from positive ions slowly drifting in the direction of the cathode, see Eq. (5.41) and Fig. 5.8. If the anode signal is read out with a high-time-resolution oscilloscope or with a fast analogue-to-digital converter (flash ADC), the ionisation structure of the particle track can also be resolved in the multiwire proportional chamber.

The time development of the avalanche formation in a multiwire proportional chamber can be detailed as follows (Fig. 7.3). A primary electron drifts towards the anode (a), the electron is accelerated in the strong electric field in the vicinity of the wire in such a way that it can gain a sufficient amount of energy on its path between two collisions so that it can ionise further gas atoms. At this moment the avalanche formation starts (b). Electrons and positive ions are created in the ionisation processes essentially in the same place. The multiplication of charge carriers comes to an end when the space charge of positive ions reduces the external electric field below a critical value. After the production of charge carriers, the electron and ion clouds drift apart (c). The electron cloud drifts in the direction of the wire and broadens slightly due to lateral diffusion. Depending on the direction of incidence of the primary electron, a slightly asymmetric density distribution of secondary electrons around the wire will be formed. This asymmetry is even more pronounced in streamer tubes. In this case, because of the use of thick anode wires and also because of the strong absorption of photons, the avalanche formation is completely restricted to the side of the anode wire where the electron was incident (see also Figs. 5.7 and 5.13) (d). In a last step the ion cloud recedes radially and slowly drifts to the cathode (e).

In most cases gold-plated tungsten wires with diameters between 10 μm and 30 μm are used as anodes. A typical anode-wire distance is 2 mm. The distance between the anode wire and the cathode is on the order of 10 mm. The individual anode wires act as independent detectors. The cathodes can be made from metal foils or also as layers of stretched wires.

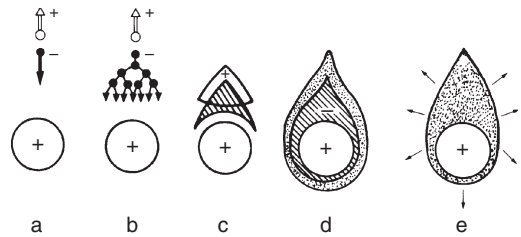

Fig. 7.3. Temporal and spatial development of an electron avalanche.

https://doi.org/10.1017/9781009401531.010 Published online by Cambridge University Press

As *counting gases* all gases and gas mixtures, which also are standard for the operation of proportional counters, namely, noble gases like Ar, Xe with admixtures of CO_2, CH_4, isobutane, and other hydrocarbons can be used [7–9]. Typical gas amplifications of 10^5 are achieved in multiwire proportional chambers. To obtain fast signals, gases with high electron mobility are used. For example, in the work of [10] a time resolution of 4.1 ns was achieved with a proportional chamber using a $CF_4 + 10\%$ i-C_4H_{10} filling.

In most chambers the possibility to process the analogue information on the wires is not taken advantage of. Instead, only thresholds for the incoming signals are set. In this mode of operation the multiwire proportional chamber is only used as a track detector. For an anode-wire distance of $d = 2\,\text{mm}$ the root-mean-square deviation of the spatial resolution is given by, see Eq. (2.6),

$$\sigma(x) = \frac{d}{\sqrt{12}} = 577\,\mu\text{m} \ . \tag{7.3}$$

The fundamental reason that limits a reduction of the wire spacing d is the *electrostatic repulsion* between long anode wires. This effect should be taken into account for MWPC construction. The central wire position is stable only if the *wire tension* T satisfies the relation

$$V \leq \frac{d}{lC}\sqrt{4\pi\varepsilon_0 T} \ , \tag{7.4}$$

where V is the anode voltage, d the wire spacing, l the wire length and C the capacitance per unit length of the detector [11, 12], Formula (7.2) (see Fig. 7.1). Using this equation, the required wire tension for stable wires can be calculated taking into account Eq. (7.2),

$$T \geq \left(\frac{V \cdot l \cdot C}{d}\right)^2 \cdot \frac{1}{4\pi\varepsilon_0} \tag{7.5}$$

$$\geq \left(\frac{V \cdot l}{d}\right)^2 \cdot 4\pi\varepsilon_0 \left[\frac{1}{2\left(\frac{\pi L}{d} - \ln\frac{2\pi r_\text{i}}{d}\right)}\right]^2 \ . \tag{7.6}$$

For a wire length $l = 1\,\text{m}$, an anode voltage $V = 5\,\text{kV}$, an anode–cathode distance of $L = 10\,\text{mm}$, an anode-wire spacing of $d = 2\,\text{mm}$ and an anode-wire diameter of $2r_\text{i} = 30\,\mu\text{m}$, Eq. (7.6) yields a minimum mechanical wire tension of 0.49 N corresponding to a stretching of the wire with a mass of about 50 g.

Longer wires must be stretched with larger forces or, if they cannot withstand higher tensions, they must be supported at fixed distances. This will, however, lead to locally inefficient zones.

https://doi.org/10.1017/9781009401531.010 Published online by Cambridge University Press

For a reliable operation of MWPCs it is also important that the wires do not sag too much gravitationally due to their own mass [13]. A sag of the anode wire would reduce the distance from anode to cathode, thereby reducing the homogeneity of the electric field.

A horizontally aligned wire of length l stretched with a tension T would exhibit a *sag* due to the pull of gravity of [14] (see also Problem 7.5)

$$f = \frac{\pi r_{\mathrm{i}}^2}{8} \cdot \varrho \cdot g \frac{l^2}{T} = \frac{mlg}{8T} \tag{7.7}$$

($m, l, \varrho, r_{\mathrm{i}}$ – mass, length, density and radius of the unsupported wire, g – acceleration due to gravity, and T – wire tension [in N]).

Taking our example from above, a gold-plated tungsten wire ($r_{\mathrm{i}} = 15\,\mu\mathrm{m}$; $\varrho_{\mathrm{W}} = 19.3\,\mathrm{g/cm}^3$) would develop a sag in the middle of the wire of

$$f = 34\,\mu\mathrm{m}\ , \tag{7.8}$$

which would be acceptable if the anode–cathode distance is on the order of 10 mm.

Multiwire proportional chambers provide a relatively poor spatial resolution which is on the order of $\approx 600\,\mu\mathrm{m}$. They also give only the coordinate perpendicular to the wires and not along the wires. An improvement in the performance can be obtained by a segmentation of the cathode and a measurement of the induced signals on the cathode segments. The cathode, for example, can be constructed of parallel strips, rectangular pads ('mosaic counter') or of a layer of wires (Fig. 7.4).

In addition to the anode signals, the induced signals on the cathode strips are now also recorded. The coordinate along the wire is given by the centre of gravity of the charges, which is derived from the signals induced on the cathode strips. Depending on the subdivision of the cathode, spatial resolutions along the wires of $\approx 50\,\mu\mathrm{m}$ can be achieved, using

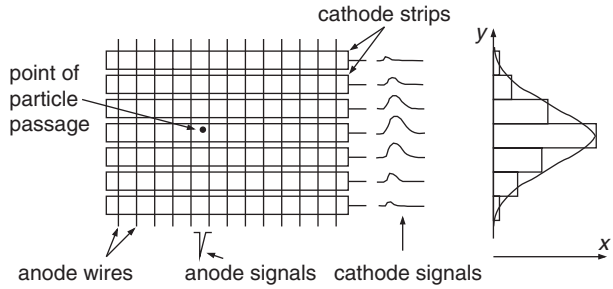

Fig. 7.4. Illustration of the cathode readout in a multiwire proportional chamber.

https://doi.org/10.1017/9781009401531.010 Published online by Cambridge University Press

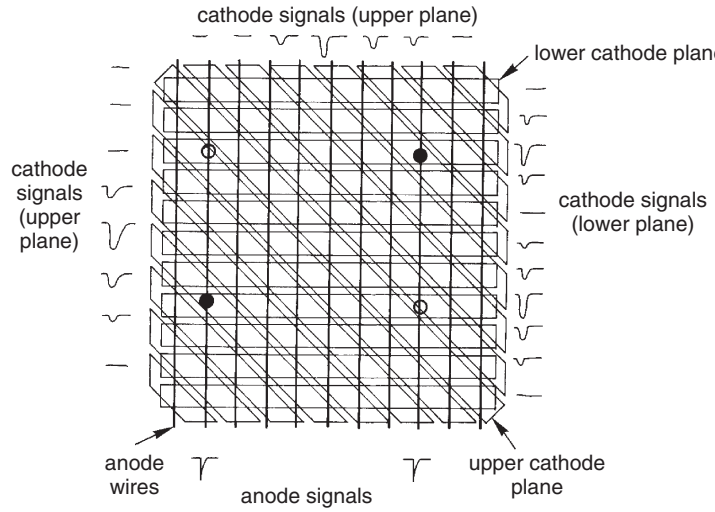

Fig. 7.5. Illustration of the resolution of ambiguities for two-particle detection in a multiwire proportional chamber.

this procedure. In case of multiple tracks also the second cathode must be segmented to exclude ambiguities.

Figure 7.5 sketches the passage of two particles through a multiwire proportional chamber. If only one cathode were segmented, the information from the anode wires and cathode strips would allow the reconstruction of four possible track coordinates, two of which, however, would be 'ghost coordinates'. They can be excluded with the help of signals from a second segmented cathode plane. A larger number of simultaneous particle tracks can be successfully reconstructed if cathode pads instead of cathode strips are used. Naturally, this results also in an increased number of electronic channels.

Further progress in the position resolution of MWPCs as well as in the *rate capability* has been achieved with the development of gaseous micropattern chambers. These detectors are discussed in Sect. 7.4.

7.2 Planar drift chambers

The principle of a *drift chamber* is illustrated by Fig. 7.6. The time Δt between the moment of the particle passage through the chamber and the arrival time of the charge cloud at the anode wire depends on the point of passage of the particle through the chamber. If v^- is the constant drift velocity of the electrons, the following linear relation holds:

$$x = v^- \cdot \Delta t \tag{7.9}$$

https://doi.org/10.1017/9781009401531.010 Published online by Cambridge University Press

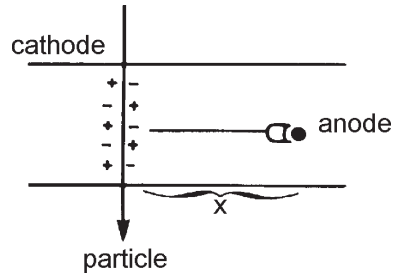

Fig. 7.6. Working principle of a drift chamber.

or, if the *drift velocity* varies along the drift path,

$$x = \int v^{-}(t)\,\mathrm{d}t \ . \tag{7.10}$$

In order to produce a suitable drift field, potential wires are introduced between neighbouring anode wires.

The measurement of the drift time allows the number of anode wires in a drift chamber to be reduced considerably in comparison to an MWPC or, by using small anode-wire spacings, to improve significantly the *spatial resolution*. Normally, both advantages can be achieved at the same time [15]. Taking a drift velocity of $v^{-} = 5\,\mathrm{cm/\mu s}$ and a time resolution of the electronics of $\sigma_t = 1\,\mathrm{ns}$, spatial resolutions of $\sigma_x = v^{-}\sigma_t = 50\,\mu\mathrm{m}$ can be achieved. However, the spatial resolution has contributions not only from the time resolution of the electronics, but also from the diffusion of the drifting electrons and the fluctuations of the statistics of primary ionisation processes. The latter are most important in the vicinity of the anode wire (Fig. 7.7 [5, 16]).

For a particle trajectory perpendicular to the chamber, the statistical production of electron–ion pairs along the particle track becomes important. The electron–ion pair closest to the anode wire is not necessarily produced on the connecting line between anode and potential wire. Spatial fluctuations of charge-carrier production result in large drift-path differences for particle trajectories close to the anode wire while they have only a minor effect for distant particle tracks (Fig. 7.8).

Naturally, the time measurement cannot discriminate between particles having passed the anode wire on the right- or on the left-hand side. A double layer of drift cells where the layers are staggered by half a cell width can resolve this *left–right ambiguity* (Fig. 7.9).

Drift chambers can be made very large [17–19]. For larger drift volumes the potential between the anode-wire position and the negative potential

https://doi.org/10.1017/9781009401531.010 Published online by Cambridge University Press

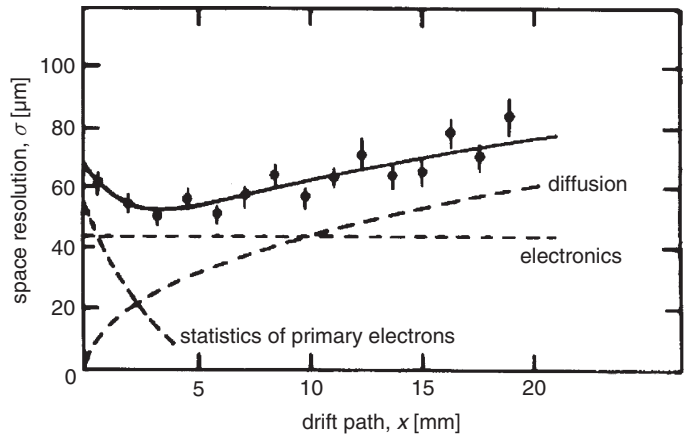

Fig. 7.7. Spatial resolution in a drift chamber as a function of the drift path [5, 16].

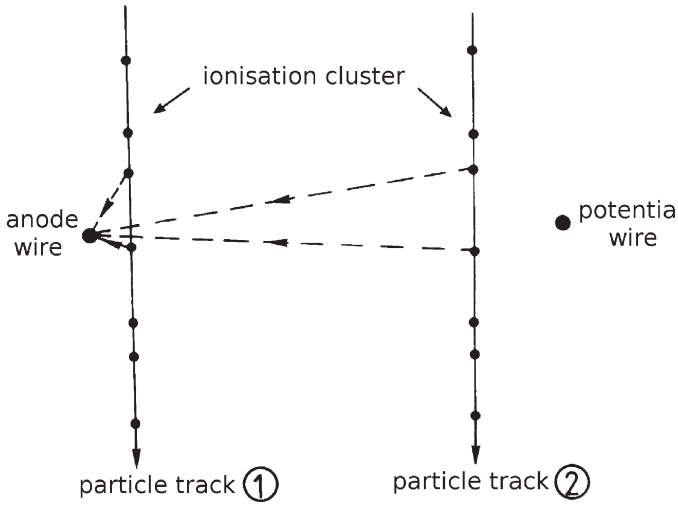

Fig. 7.8. Illustration of different drift paths for 'near' and 'distant' particle tracks to explain the dependence of the spatial resolution on the primary ionisation statistics.

on the chamber ends is divided linearly by using cathode strips connected to a chain of resistors (Fig. 7.10).

The maximum achievable spatial resolution for large-area drift chambers is limited primarily by mechanical tolerances. For large chambers typical values of 200 μm are obtained. In small chambers ($10 \times 10\,\mathrm{cm}^2$) spatial resolutions of 20 μm have been achieved. In the latter case the time resolution of the electronics and the diffusion of electrons on their way to

https://doi.org/10.1017/9781009401531.010 Published online by Cambridge University Press

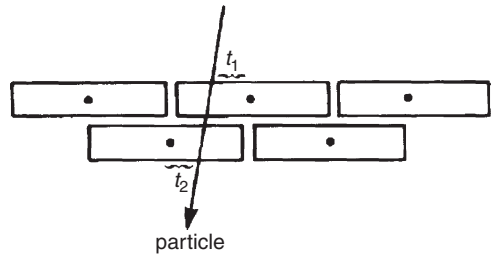

Fig. 7.9. Resolution of the left–right ambiguity in a drift chamber.

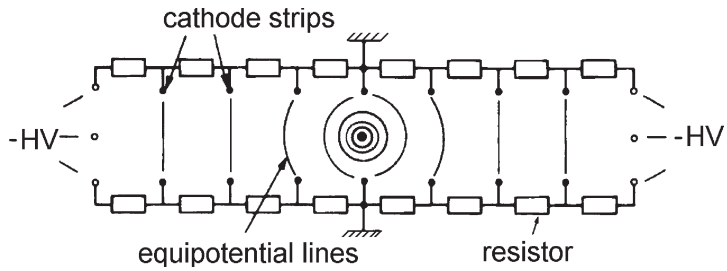

Fig. 7.10. Illustration of the field formation in a large-area drift chamber.

the anode are the main limiting factors. The determination of the coordinate along the wires can again be performed with the help of cathode pads.

The relation between the drift time t and the drift distance in a large-area ($80 \times 80\,\mathrm{cm}^2$) drift chamber with only one anode wire is shown in Fig. 7.11 [19]. The chamber was operated with a gas mixture of 93% argon and 7% isobutane.

Field formation in large-area drift chambers can also be achieved by the attachment of positive ions on insulating chamber surfaces. In these chambers an insulating foil is mounted on the large-area cathode facing the drift space (Fig. 7.12). In the time shortly after the positive high voltage on the anode wire has been switched on, the field quality is insufficient to expect a reasonable electron drift with good spatial resolution over the whole chamber volume (Fig. 7.13a). Positive ions which have been produced by the penetrating particle now start to drift along the field lines to the electrodes. The electrons will be drained by the anode wire, but the positive ions will get stuck on the inner side of the insulator on the cathode thereby forcing the field lines out of this region. After a certain while ('charging-up time') no field lines will end on the covers of the chamber and an ideal drift-field configuration will have been formed (Fig. 7.13b, [20, 21]). If the chamber walls are not completely insulating, i.e., their volume or surface resistance is finite, some field lines will still

https://doi.org/10.1017/9781009401531.010 Published online by Cambridge University Press

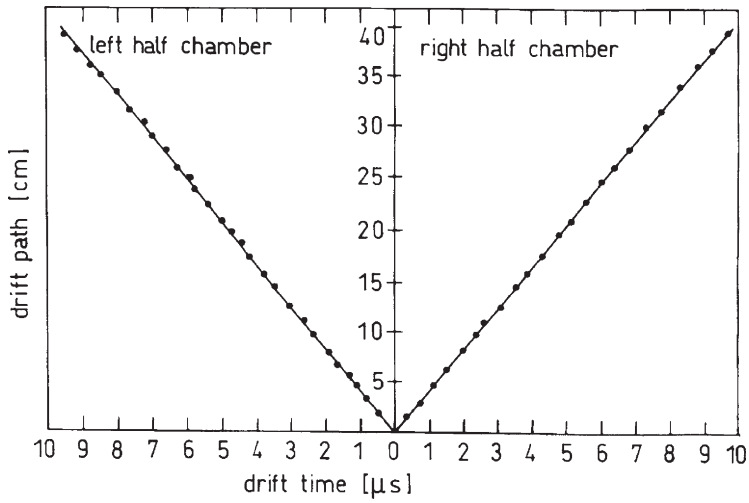

Fig. 7.11. Drift-time–space relation in a large drift chamber ($80 \times 80\,\mathrm{cm}^2$) with only one anode wire [19].

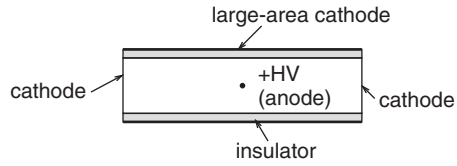

Fig. 7.12. Principle of construction of an *electrodeless drift chamber.*

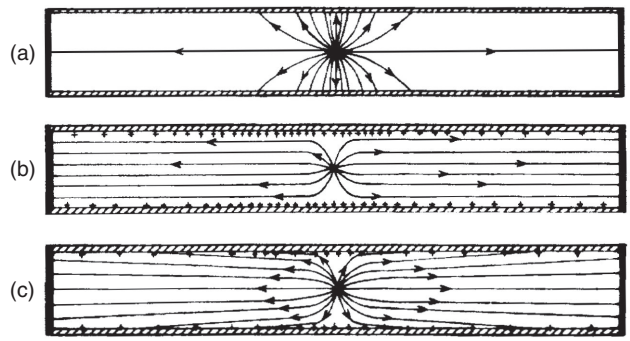

Fig. 7.13. Field formation in an electrodeless drift chamber by ion attachment [20, 21].

end on the chamber covers (Fig. 7.13c). Although, in this case, no ideal field quality is achieved, an overcharging of the cathodes is avoided since the chamber walls have a certain conductivity or transparency to allow for a removal of surplus surface charges.

https://doi.org/10.1017/9781009401531.010 Published online by Cambridge University Press

Initial difficulties with long charging times ($\approx$ 1 h) and problems of overcharging of the insulators at high rates can be overcome by a suitable choice of dielectrics on the cathodes [22]. Based on this principle chambers of very different geometry (rectangular chambers, cylindrical chambers, drift tubes, etc.) even with long drift paths ($>$ 1 m) have been constructed [23–26].

The principle of electron drift in drift chambers can be used in many different ways. The introduction of a grid into a drift chamber enables the separation of the drift volume proper from the gas amplification region. The choice of suitable gases and voltages allows very low drift velocities in the drift volume so that the ionisation structure of a track of a charged particle can be electronically resolved without large expense (principle of a *time expansion chamber*) [27, 28]. The use of very small anode-wire distances also allows high counting rates per unit area because the rate per wire in this case stays within reasonable limits.

The *induction drift chamber* [29–31] also allows high spatial resolutions by using anode and potential wires with small relative distances. The formation of an electron avalanche on the anode will induce charge signals on neighbouring pickup electrodes which allow at the same time the determination of the angle of incidence of a particle and the resolution of the right–left ambiguity. Because of the small anode spacing the induction drift chamber is also an excellent candidate for high-rate experiments, for example, for the investigation of electron–proton interactions in a storage ring at high repetition frequencies (e.g. in HERA, the hadron–electron storage ring at the German electron synchrotron DESY). Particle rates up to $10^6\,\mathrm{mm^{-2}\,s^{-1}}$ can be processed.

The finite drift time can also be taken advantage of to decide whether or not an event in a detector is of interest. This, for example, can be realised in the *multistep avalanche chamber*. Figure 7.14 shows the

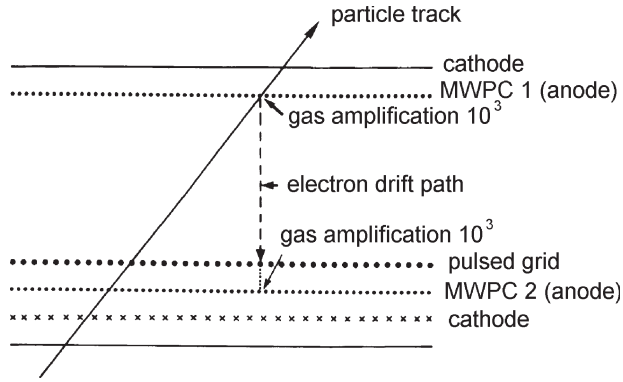

Fig. 7.14. Principle of operation of a multistep avalanche chamber [32].

https://doi.org/10.1017/9781009401531.010 Published online by Cambridge University Press

principle of operation [32]. The detector consists of two multiwire proportional chambers (MWPC 1 and 2), whose gas amplifications are arranged to be relatively small ($\approx 10^3$). All particles penetrating the detector will produce relatively weak signals in both proportional chambers. Electrons from the avalanche in MWPC 1 can be transferred with a certain probability into the drift region situated between the two chambers. Depending on the width of the drift space these electrons require several hundred nanoseconds to arrive at the second multiwire proportional chamber. The end of the drift space is formed by a wire grid which is only opened by a voltage signal if some external logic signals an interesting event. In this case the drifting electrons are again multiplied by a gas amplification factor 10^3 so that a gas amplification of $10^6 \cdot \varepsilon$ in MWPC 2 is obtained, where ε is the mean transfer probability of an electron produced in chamber 1 into the drift space. If ε is sufficiently large (e.g. >0.1), the signal in chamber 2 will be large enough to trigger the conventional readout electronics of this chamber. These 'gas delays', however, are nowadays mainly realised by purely electronic delay circuits.

Experiments at electron–positron storage rings and at future proton–proton colliders require large-area chambers for muon detection. There are many candidates for muon chambers, such as layers of streamer tubes. For the accurate reconstruction of decay products of the searched-for Higgs particles, for example, excellent spatial resolutions over very large areas are mandatory. These conditions can be met with modular drift chambers [33, 34].

7.3 Cylindrical wire chambers

For storage-ring experiments cylindrical detectors have been developed which fulfill the requirement of a maximum solid-angle coverage, i.e. *hermeticity*. In the very first experiments cylindrical multigap spark chambers (see Chap. 6) and multiwire proportional chambers were used, however, at present drift chambers have been almost exclusively adopted for the measurement of particle trajectories and the determination of the specific ionisation of charged particles.

There are several types of such detectors: cylindrical drift chambers whose wire layers form cylindrical surfaces; jet chambers, where the drift spaces are segmented in azimuthal direction; and time-projection chambers, which are in the sensitive volume free of any material (apart from the counting gas), and where the information on particle trajectories is drifted to circular end-plate detectors.

Cylindrical drift chambers operated in a magnetic field allow the determination of the momenta of charged particles. The transverse momentum

p of charged particles is calculated from the axial magnetic field and the bending radius of the track, ρ, to be (see Chap. 11)

$$p\,[\mathrm{GeV}/c] = 0.3\ B\,[\mathrm{T}] \cdot \rho\,[\mathrm{m}]\ . \tag{7.11}$$

7.3.1 Cylindrical proportional and drift chambers

Figure 7.15 shows the principle of construction of a *cylindrical drift chamber*. All wires are stretched in an axial direction (in the z direction, the direction of the magnetic field). For cylindrical drift chambers a potential wire is stretched between two anode wires. Two neighbouring readout layers are separated by a cylindrical layer of potential wires. In the most simple configuration the individual drift cells are trapezoidal where the boundaries are formed by eight potential wires. Figure 7.15 shows a projection in the $r\varphi$ plane, where r is the distance from the centre of the chamber and φ is the azimuthal angle. Apart from this trapezoidal drift cell other drift-cell geometries are also in use [35].

In the so-called *open trapezoidal cells* every second potential wire on the potential-wire planes is left out (Fig. 7.16).

The field quality can be improved by using closed cells (Fig. 7.17) at the expense of a larger number of wires. The compromise between the aforementioned drift-cell configurations is a hexagonal structure of the cells (Fig. 7.18). In all these configurations the potential wires are of larger diameter ($\varnothing \approx 100\,\mu\mathrm{m}$) compared to the anode wires ($\varnothing \approx 30\,\mu\mathrm{m}$).

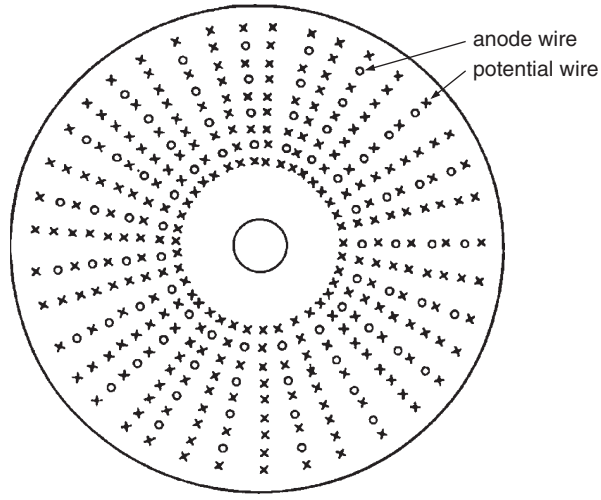

Fig. 7.15. Schematic layout of a cylindrical drift chamber. The figure shows a view of the chamber along the wires.

https://doi.org/10.1017/9781009401531.010 Published online by Cambridge University Press

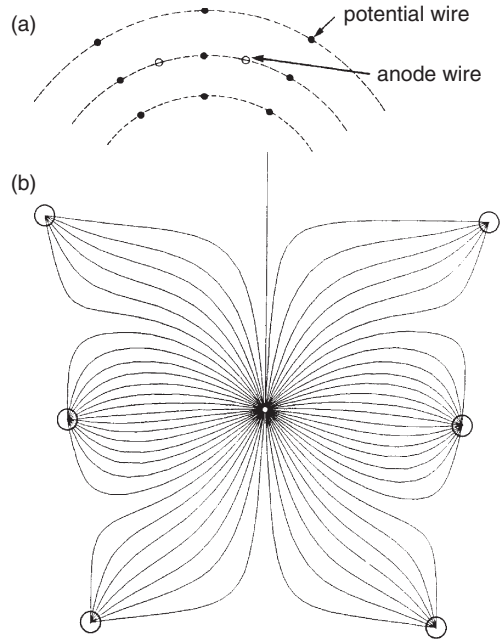

Fig. 7.16. (a) Illustration of an open drift-cell geometry. (b) Field lines in an open drift cell [36].

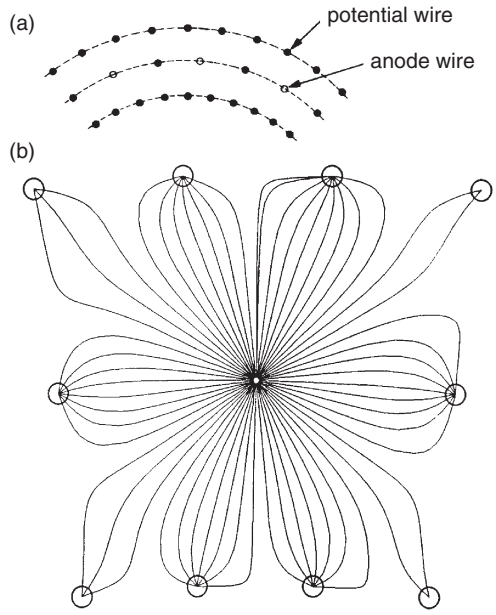

Fig. 7.17. (a) Illustration of a closed drift-cell geometry. (b) Field lines in a closed drift cell [36].

https://doi.org/10.1017/9781009401531.010 Published online by Cambridge University Press

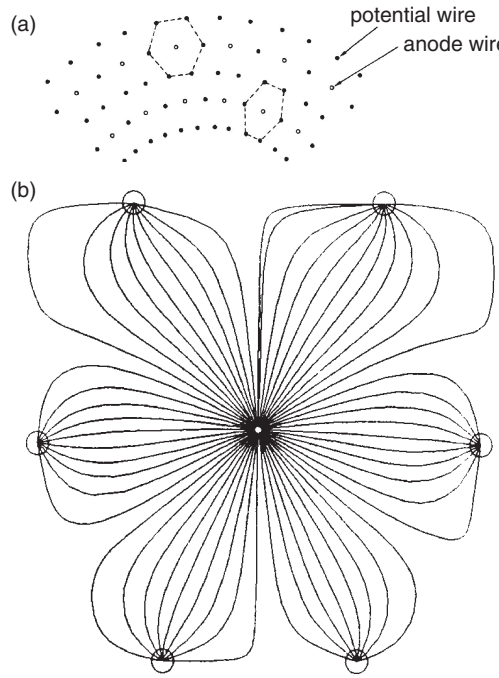

Fig. 7.18. (a) Hexagonal drift-cell geometry. (b) Field lines in a hexagonal drift cell [36].

All wires are stretched between two end plates which must take the whole wire tension. For large cylindrical wire chambers with several thousand anode and potential wires this tension can amount to several tons.

The configurations described so far do not allow a determination of the coordinate along the wire. Since it is impossible to segment the cathode wires in these configurations, other methods to determine the coordinate along the wire have been developed. One way of determining the z coordinate is the *charge-division method* that requires to measure the signals arriving at both ends of the anode wire. Since the wire has a certain resistivity (typically 5–10 Ω/cm), the charges received at the ends depend on the position of the avalanche. Then the ratio $(q_1 - q_2)/(q_1 + q_2)$ (q_1 and q_2 are the corresponding charges) determines the point of particle intersection [37, 38]. Equally well, the propagation times of signals on the anode wires can be measured at both ends. The charge-division technique allows accuracies on the order of 1% of the wire length. This precision can also be obtained with fast electronics applied to the propagation-time technique.

Another method for measuring the position of the avalanche along the sense wire uses *spiral-wire delay lines*, of diameter smaller than 2 mm, stretched parallel to the sense wire [39]. This technique, which

https://doi.org/10.1017/9781009401531.010 Published online by Cambridge University Press

is mechanically somewhat complicated for large detector systems, allows accuracies on the order of 0.1% along the wires. If the delay line is placed between two closely spaced wires, it also resolves the left–right ambiguity. More sophisticated delay-line readouts allow even higher spatial resolutions [40, 41].

However, there is also a fourth possibility by which one can determine the z coordinate along the wire. In this case, some anode wires are stretched not exactly parallel to the cylinder axis, but are tilted by a small angle with respect to this axis (*stereo wires*). The spatial resolution $\sigma_{r,\varphi}$ measured perpendicular to the anode wires is then translated into a resolution σ_z along the wire according to

$$\sigma_z = \frac{\sigma_{r,\varphi}}{\sin\gamma} \ , \tag{7.12}$$

if γ is the 'stereo angle' (Fig. 7.19). For typical $r\varphi$ resolutions of 200 µm z resolutions on the order of $\sigma_z = 3$ mm are obtained, if the stereo angle is $\gamma \approx 4°$. In this case, the z resolution does not depend on the wire length. The magnitude of the stereo angle is limited by the maximum allowed transverse cell size. Cylindrical drift chambers with stereo wires are also known as *hyperbolic chambers*, because the tilted stereo wires appear to sag hyperbolically with respect to the axial anode wires.

In all these types of chambers, where the drift field is perpendicular to the magnetic field, special attention must be paid to the Lorentz angle (see Sect. 1.4).

Figure 7.20 shows the drift trajectories of electrons in an open rectangular drift cell with and without an axial magnetic field [42, 43].

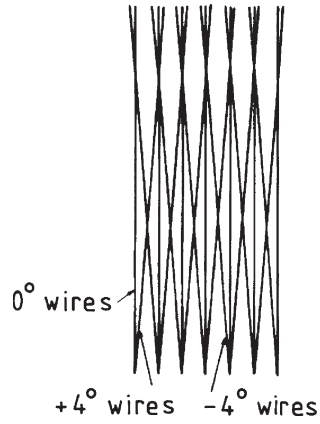

Fig. 7.19. Illustration of the determination of the coordinate along the anode wire by use of stereo wires.

https://doi.org/10.1017/9781009401531.010 Published online by Cambridge University Press

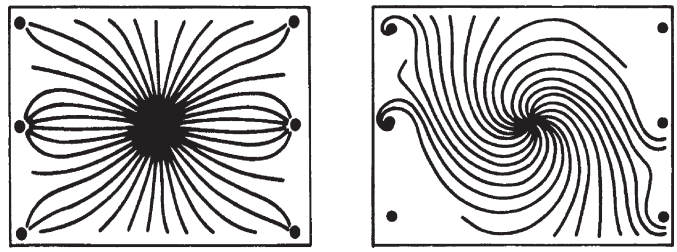

Fig. 7.20. Drift trajectories of electrons in an open rectangular drift cell (a) without and (b) with magnetic field [42, 43].

Figure 7.21 shows the $r\varphi$ projections of reconstructed particle tracks from an electron–positron interaction (PLUTO) in a cylindrical multiwire proportional chamber [44]. Figure 7.21a shows a clear two-jet structure which originated from the process $e^+e^- \rightarrow q\bar{q}$ (production of a quark–antiquark pair). Part (b) of this figure exhibits a particularly interesting event of an electron–positron annihilation from the aesthetic point of view. The track reconstruction in this case was performed using only the fired anode wires without making use of drift-time information (see Sect. 7.1). The spatial resolutions obtained in this way, of course, cannot compete with those that can be reached in drift chambers.

Cylindrical multiwire proportional chambers can also be constructed from layers of so-called *straw chambers* (Fig. 7.22) [45–49]. Such straw-tube chambers are frequently used as vertex detectors in storage-ring experiments [50, 51]. These straw chambers are made from thin aluminised mylar foils. The straw tubes have diameters of between 5 mm and 10 mm and are frequently operated at overpressure. These detectors allow for spatial resolutions of 30 μm.

Due to the construction of these chambers the risk of broken wires is minimised. In conventional cylindrical chambers a single broken wire can disable large regions of a detector [52]. In contrast, in straw-tube chambers only the straw with the broken wire is affected.

Because of their small size straw-tube chambers are candidates for high-rate experiments [53]. Due to the short electron drift distance they can also be operated in high magnetic fields without significant deterioration of the spatial resolution [54].

Very compact configurations with high spatial resolution can also be obtained with *multiwire drift modules* (Fig. 7.23) [51, 55, 56].

In the example shown, 70 drift cells are arranged in a hexagonal structure of 30 mm diameter only. Figure 7.24 shows the structure of electric field and equipotential lines for an individual drift cell [55]. Figure 7.25 shows a single particle track through such a multiwire drift module [55].

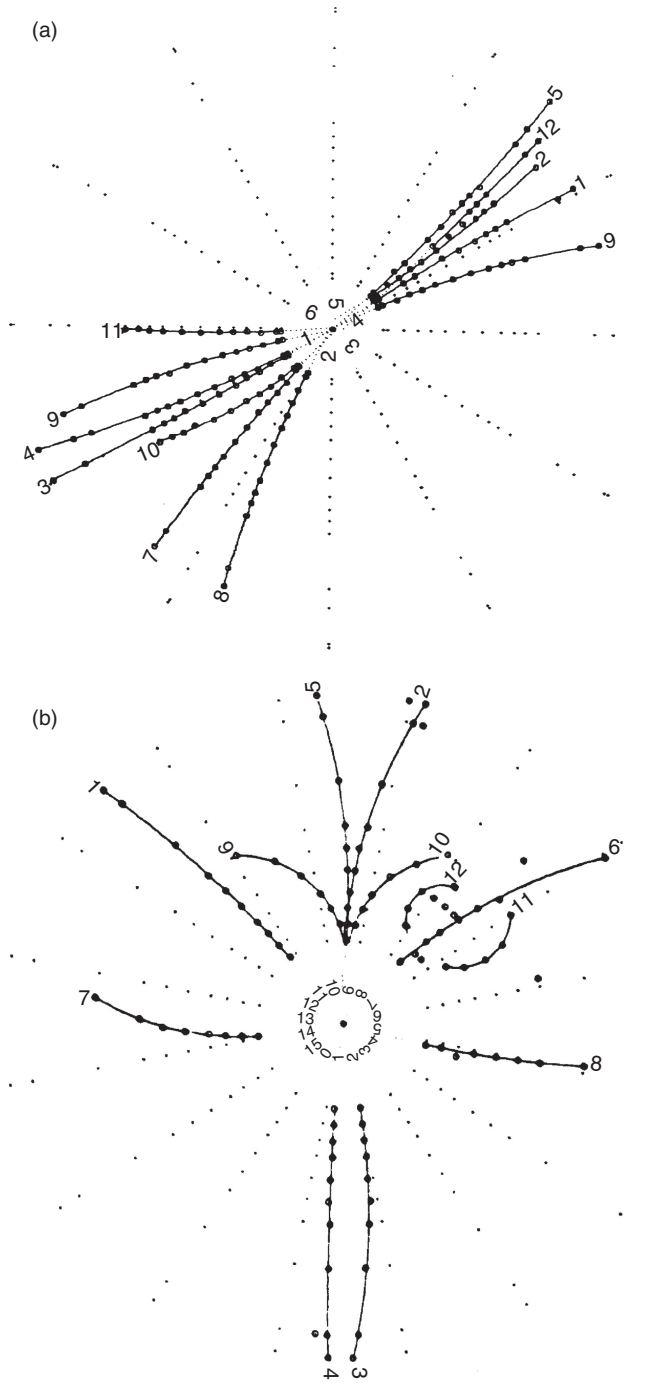

Fig. 7.21. Multitrack events of electron–positron interactions measured in the PLUTO central detector [44].

https://doi.org/10.1017/9781009401531.010 Published online by Cambridge University Press

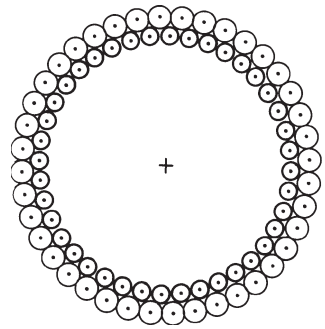

Fig. 7.22. Cylindrical configuration of thin-wall straw-tube chambers [45, 47].

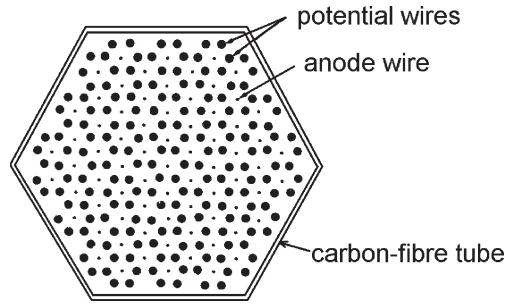

Fig. 7.23. Schematic representation of a multiwire drift module. In this hexagonal structure each anode wire is surrounded by six potential wires. Seventy drift cells are incorporated in one container of 30 mm diameter only, which is made from carbon-fibre material [55].

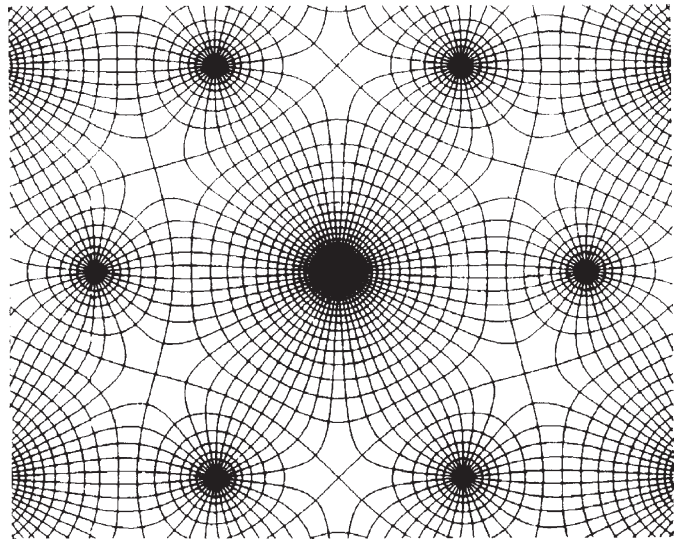

Fig. 7.24. Calculated electric field and equipotential lines in one individual hexagonal drift cell of the multiwire drift module [55].

https://doi.org/10.1017/9781009401531.010 Published online by Cambridge University Press

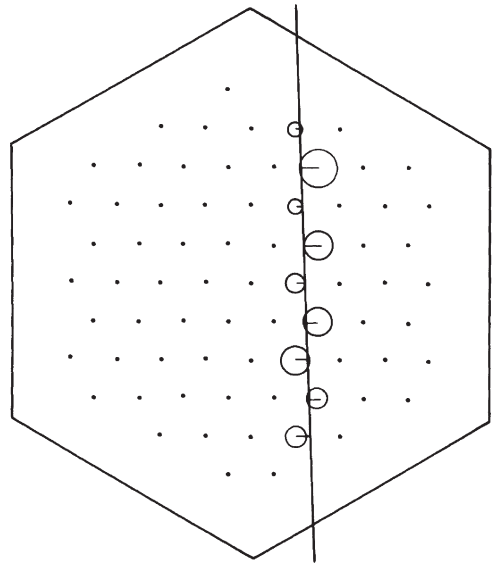

Fig. 7.25. Example of a single particle passage through a multiwire drift module. The circles indicate the measured drift times of the fired anode wires. The particle track is a tangent to all drift circles [55].

7.3.2 Jet drift chambers

Cylindrical drift chambers used now at collider experiments have up to 50 layers of anode wires. These are often used for multiple $\mathrm{d}E/\mathrm{d}x$ measurements, e.g. to discriminate charged pions against kaons.

In *jet drift chambers*, especially suited for these tasks, an accurate measurement of the energy loss by ionisation is performed by determining the specific ionisation on as large a number of anode wires as possible. The central detector of the JADE experiment [57, 58] at PETRA determined the energy loss of charged particles on 48 wires, which are stretched parallel to the magnetic field. The cylindrical volume of the drift chamber is subdivided into 24 radial segments. Figure 7.26 sketches the principle of the arrangement of one of these sectors, which is itself again subdivided into smaller drift regions of 16 anode wires each.

The field formation is made by potential strips at the boundaries between two sectors. The electric field is perpendicular to the counting-wire planes and also perpendicular to the direction of the magnetic field. For this reason the electron drift follows the *Lorentz angle* which is determined from the electric and magnetic field strengths and the drift velocity. For the solenoidal $\vec{B}$ field of 0.45 T in JADE a Lorentz angle of $\alpha = 18.5°$ is obtained. To reach a maximum accuracy for an individual energy-loss measurement the chamber is operated under a pressure of 4 atm. This

https://doi.org/10.1017/9781009401531.010 Published online by Cambridge University Press

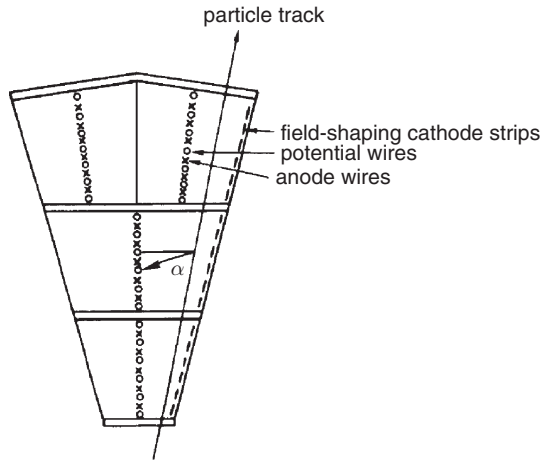

Fig. 7.26. Segment of a jet drift chamber (after [35, 57–59]). The field-forming cathode strips are only shown on one side of the segment (for reasons of simplicity and not to overload the figure the two inner rings 1 and 2 show only five and the outer ring 3 only six anode wires).

overpressure also suppresses the influence of primary ion statistics on the spatial resolution. However, it is important not to increase the pressure to too high a value since the logarithmic rise of the energy loss, which is the basis for particle separation, may be reduced by the onset of the density effect.

The determination of the coordinate along the wire is done by using the charge-division method.

The $r\varphi$ projection of trajectories of particles from an electron–positron interaction in the JADE drift chamber is shown in Fig. 7.27 [57, 58]. The 48 coordinates along each track originating from the interaction vertex can clearly be recognised. The left–right ambiguity in this chamber is resolved by staggering the anode wires (see also Fig. 7.28). An even larger jet drift chamber was mounted in the OPAL detector at the Large Electron–Positron collider LEP at CERN [60].

The structure of the MARK II jet chamber (Fig. 7.28 [61, 62]) is very similar to that of the JADE chamber. The ionisation produced by particle tracks in this detector is collected on the anode wires. Potential wires between the anodes and layers of field-forming wires produce the drift field. The field quality at the ends of the drift cell is improved by additional potential wires. The drift trajectories in this jet chamber in the presence of the magnetic field are shown in Fig. 7.29 [61, 62].

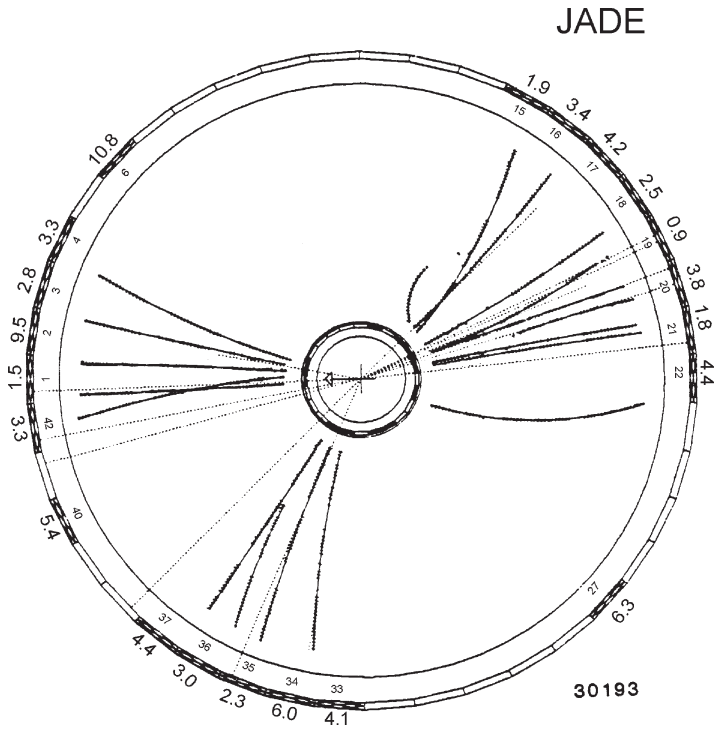

Fig. 7.27. The $r\varphi$ projection of interaction products from an electron–positron collision (gluon production: $e^+ + e^- \to q + \bar{q} + g$, producing three jets) in the JADE central detector [57, 58]. The bent tracks correspond to charged particles and the dotted tracks to neutral particles which are not affected by the magnetic field (and are not registered in the chamber).

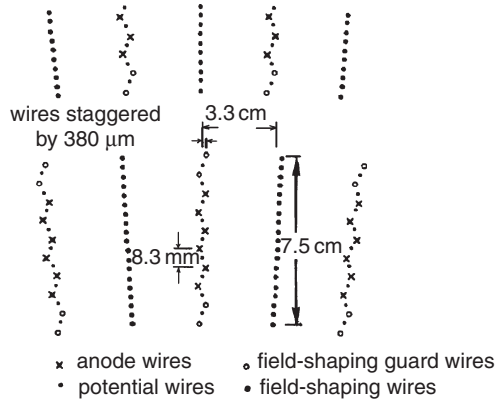

Fig. 7.28. Drift-cell geometry of the MARK II jet drift chamber [61, 62].

https://doi.org/10.1017/9781009401531.010 Published online by Cambridge University Press

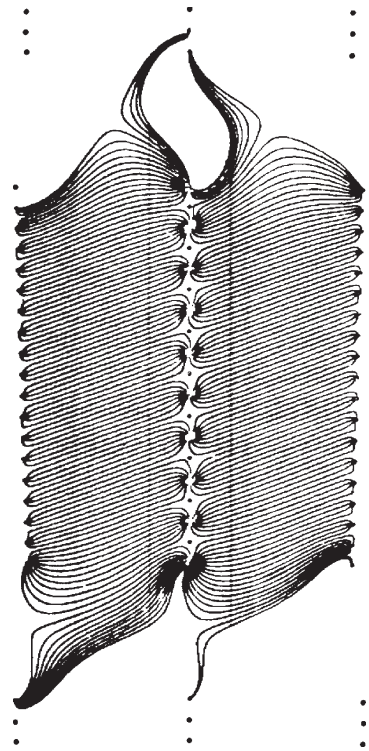

Fig. 7.29. Calculated drift trajectories in a jet-chamber drift cell in the presence of a magnetic field [61, 62].

7.3.3 Time-projection chambers (TPCs)

The *crème de la crème* of track recording in cylindrical detectors (also suited for other geometries) at the moment is realised with the *time-projection chamber* [63]. Apart from the counting gas this detector contains no other constructional elements and thereby represents the optimum as far as minimising multiple scattering and photon conversions are concerned [64]. A side view of the construction principle of a time-projection chamber is shown in Fig. 7.30.

The chamber is divided into two halves by means of a central electrode. A typical counting gas is a mixture of argon and methane (90:10).

The primary ionisation produced by charged particles drifts in the electric field – which is typically parallel to the magnetic field – in the direction of the end plates of the chamber, which in most cases consist of multiwire proportional detectors. The magnetic field suppresses the diffusion perpendicular to the field. This is achieved by the action of the magnetic forces on the drifting electrons which, as a consequence, spiral around the

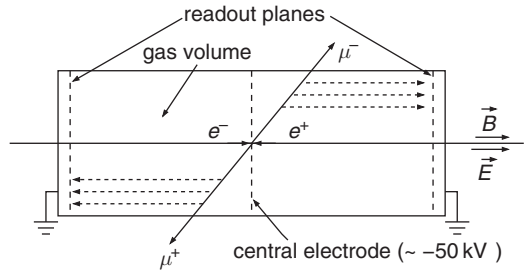

Fig. 7.30. Working principle of a time-projection chamber (TPC) [63] for a collider experiment. For simplicity the beam pipe is not shown.

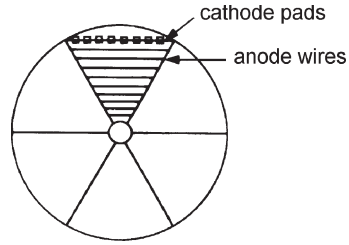

Fig. 7.31. Principle of operation of a pad readout in an endcap multiwire proportional chamber. The anode wires and some cathode pads are shown for one sector.

direction of the magnetic field. For typical values of electric and magnetic field strengths, Larmor radii below 1 μm are obtained. The arrival time of primary electrons at the end plates supplies the z coordinate along the cylinder axis. The layout of one end plate is sketched in Fig. 7.31.

The gas amplification of the primary ionisation takes place at the anode wires, which are stretched in azimuthal direction. The radial coordinate r can in principle be obtained from the fired wire (for short wires). To obtain three-dimensional coordinates the cathodes of endcap-multiwire-proportional-chamber segments are usually structured as pads. Therefore the radial coordinate is also provided by reading the position of the fired pad. In addition, the pads supply the coordinate along the anode wire resulting in a determination of the azimuthal angle φ. Therefore, the time-projection chamber allows the determination of the coordinates r, φ and z, i.e. a three-dimensional space point, for each cluster of primary electrons produced in the ionisation process.

The analogue signals on the anode wires provide information on the specific energy loss and can consequently be used for particle identification. Typical values of the magnetic field are around 1.5 T, and around

https://doi.org/10.1017/9781009401531.010 Published online by Cambridge University Press

20 kV/m for the electric field. Since in this construction electric and magnetic field are parallel, the Lorentz angle is zero and the electrons drift parallel to $\vec{E}$ and $\vec{B}$ (there is no '$\vec{E} \times \vec{B}$ effect').

A problem, however, is caused by the large number of positive ions which are produced in the gas amplification process at the end plates and which have to drift a long way back to the central electrode. The strong space charge of the drifting positive ions causes the field quality to deteriorate. This can be overcome by introducing an additional grid ('gate') between the drift volume and the endcap multiwire proportional chamber (Fig. 7.32).

The gate is normally closed. It is only opened for a short period of time if an external trigger signals an interesting event. In the closed state the gate prevents ions from drifting back into the drift volume. Thereby the quality of the electric field in the sensitive detector volume remains unchanged [35]. This means that the gate serves a dual purpose. On the one hand, electrons from the drift volume can be prevented from entering the gas amplification region of the endcap multiwire proportional chamber if there is no trigger which would signal an interesting event. On the other hand – for gas-amplified interesting events – the positive ions are prevented from drifting back into the detector volume. Figure 7.33 shows the operation principle of the gate in the ALEPH TPC [65].

Time-projection chambers can be made very large (diameter ≥ 3 m, length ≥ 5 m). They contain a large number of analogue readout channels (number of anode wires ≈ 5000 and cathode pads $\approx 50\,000$). Several hundred samples can be obtained per track, which ensure an excellent determination of the radius of curvature and allow an accurate measurement of the energy loss, which is essential for particle identification [65–67]. The drawback of the time-projection chamber is the fact that high particle rates cannot be handled, because the drift time of the electrons in the detector volume amounts to 40 μs (for a drift path of 2 m) and the readout of the analogue information also requires several microseconds.

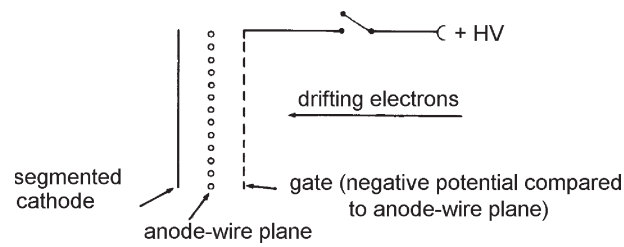

Fig. 7.32. *Gating principle* in a time-projection chamber.

https://doi.org/10.1017/9781009401531.010 Published online by Cambridge University Press

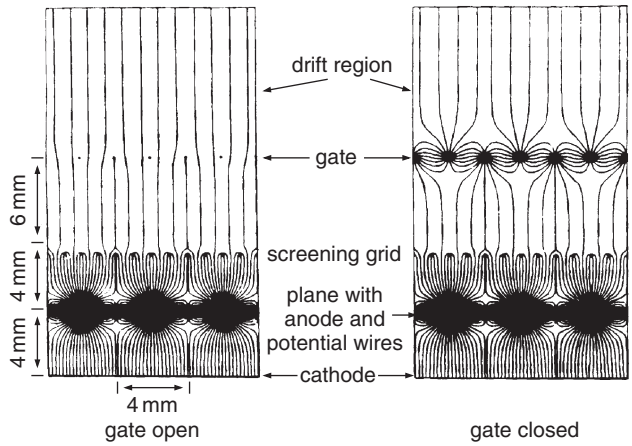

Fig. 7.33. Working principle of the gate in the ALEPH TPC [65]. For an open gate the ionisation electrons are not prevented from entering the gas amplification region. The closed gate, however, confines the positive ions to the gas amplification region. A closed gate also stops electrons in the drift volume from entering the gas-amplification region. For an event of interest the gate is first opened to allow the primary electrons to enter the gas amplification region and then it is closed to prevent the positive ions produced in the avalanche process from drifting back into the detector volume.

In large time-projection chambers typical spatial resolutions of $\sigma_z = 1\,\text{mm}$ and $\sigma_{r,\varphi} = 160\,\mu\text{m}$ are obtained. In particular, the resolution of the z coordinate requires an accurate knowledge of the drift velocity. This, however, can be calibrated and monitored by UV-laser-generated ionisation tracks.

Figure 7.34 shows the $r\varphi$ projection of an electron–positron annihilation in the ALEPH time-projection chamber [65, 66].

Time-projection chambers can also be operated with liquid noble gases. Such *liquid-argon time-projection chambers* represent an electronic replacement for bubble chambers with the possibility of three-dimensional event reconstruction. In addition, they can serve simultaneously as a calorimetric detector (see Chap. 8), are permanently sensitive, and can intrinsically supply a trigger signal by means of the scintillation light produced in the liquid noble gas (see Sect. 5.4) [68–73]. The electronic resolution of the bubble-chamber-like pictures is on the order of $100\,\mu\text{m}$. The operation of large liquid-argon TPCs, however, requires ultrapure argon (contaminants $< 0.1\,\text{ppb}$ ($1\,\text{ppb} \equiv 10^{-9}$)) and high-performance low-noise preamplifiers since no gas amplification occurs in the counting medium. Multi-kiloton liquid-argon TPCs appear to be good candidates to study rare phenomena in underground experiments ranging from the search for nucleon decay to solar-neutrino observations [74, 75].

https://doi.org/10.1017/9781009401531.010 Published online by Cambridge University Press

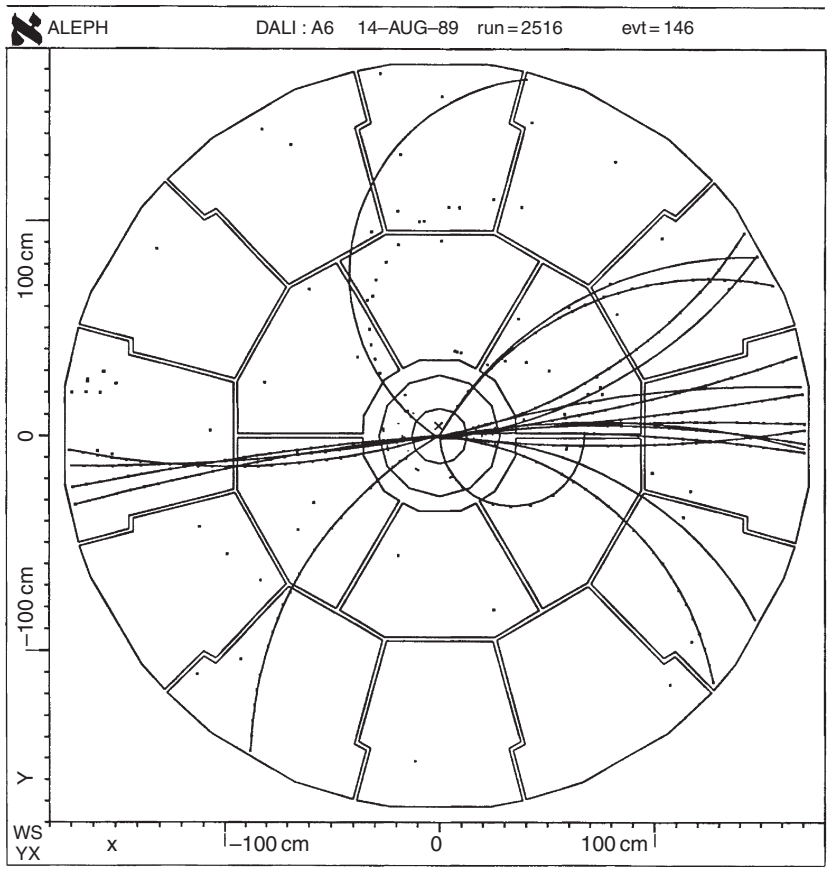

Fig. 7.34. The $r\varphi$ projection of an electron–positron annihilation in the ALEPH time-projection chamber [65, 66]. The end-plate detector is structured into two rings which are made from six (inner ring) and twelve (outer ring) multiwire-proportional-chamber segments.

Self-triggering time-projection chambers have also been operated successfully with liquid xenon [76, 77].

7.4 Micropattern gaseous detectors

The construction of multiwire proportional chambers would be simplified and their stability and flexibility would be greatly enhanced if anodes were made in the form of strips or dots on insulating or semiconducting surfaces instead of stretching anode wires in the counter volume. The rate capability improves by more than one order of magnitude for these devices

https://doi.org/10.1017/9781009401531.010 Published online by Cambridge University Press

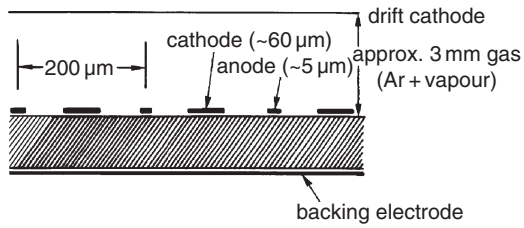

Fig. 7.35. Schematic arrangement of a microstrip gas detector.

[78, 79]. At present the class of *micropattern gaseous detectors* is already rather wide and many new promising devices are under study [80–82].

These microstrip gaseous chambers (MSGCs) are miniaturised multiwire proportional chambers, in which the dimensions are reduced by about a factor of 10 in comparison to conventional chambers (Fig. 7.35). The typical pitch is 100–200 µm and the gas gap varies between 2–10 mm. This has been made possible because the electrode structures can be reduced with the help of electron lithography. The wires are replaced by strips which are evaporated onto a thin substrate. Cathode strips arranged between the anode strips allow for an improved field quality and a fast removal of positive ions. The segmentation of the otherwise planar cathodes in the form of strips or pixels [83, 84] also permits two-dimensional readout. Instead of mounting the electrode structures on ceramic substrates, they can also be arranged on thin plastic foils. In this way, even light, flexible detectors can be constructed which exhibit a high spatial resolution. Possible disadvantages lie in the electrostatic charging-up of the insulating plastic structures which can lead to time-dependent amplification properties because of the modified electric fields [85–90].

The gain of an MSGC can be up to 10^4. The spatial resolution of this device for point-like ionisation, measured with soft X rays, reaches 20–30 µm rms. For minimum-ionising charged particles crossing the gap, the resolution depends on the angle of incidence. It is dominated by primary ionisation statistics [91].

The obvious advantages of these *microstrip detectors* – apart from their excellent spatial resolution – are the low dead time (the positive ions being produced in the avalanche will drift a very short distance to the cathode strips in the vicinity of the anodes), the reduced radiation damage (because of the smaller sensitive area per readout element) and the high-rate capability.

Microstrip proportional chambers can also be operated in the drift mode (see Sect. 7.2).

However, the MSGC appeared to be prone to ageing and discharge damages [92]. To avoid these problems many different designs of micropattern detectors were suggested. Here we consider two of them, Micromegas [93]

https://doi.org/10.1017/9781009401531.010 Published online by Cambridge University Press

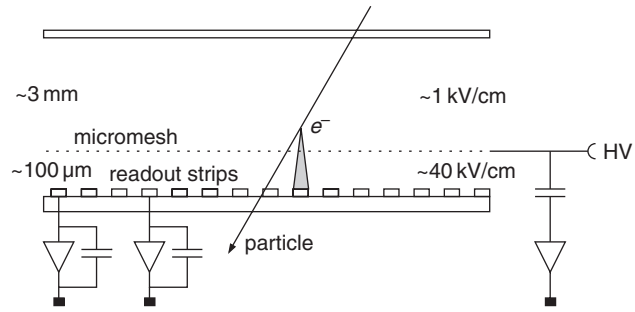

Fig. 7.36. The layout of the Micromegas detector [11, 95].

and GEM [94] detectors, widely used now by many groups. Both of them demonstrate good performance.

The *Micromegas* design is shown in Fig. 7.36. Electrons released by charged particles in the conversion gap of 2–5 mm width drift to the multiplication gap. This gap of 50–100 µm width is bordered by a fine cathode mesh and an anode readout strip or pad structure. A constant distance between cathode and anode is kept with dielectric pillars with a pitch of ≈ 1 mm.

A high electric field in the multiplication gap (30–80 kV/cm) provides a gain up to 10^5. Since most of the ions produced in the avalanche are collected by the nearby cathode, this device has excellent timing properties [96] and a high-rate capability [97].

Another structure providing charge multiplication is the *Gas Electron Multiplier* (GEM). This is a thin (≈ 50 µm) insulating kapton foil coated with a metal film on both sides. It contains chemically produced holes of 50–100 µm in diameter with 100–200 µm pitch. The metal films have different potential to allow gas multiplication in the holes. A GEM schematic view and the electric field distribution is presented in Figs. 7.37 and 7.38. A GEM-based detector contains a drift cathode separated from one or several GEM layers and an anode readout structure as shown in Fig. 7.37.

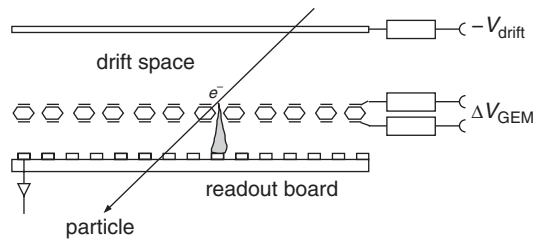

Fig. 7.37. Detailed layout of a GEM detector.

https://doi.org/10.1017/9781009401531.010 Published online by Cambridge University Press

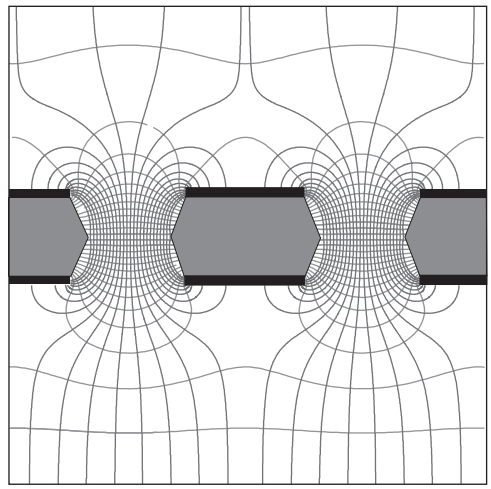

Fig. 7.38. Electric field distribution in a GEM detector [11, 94].

The electrons are guided by the electric drift field to the GEM where they experience a high electric field in the GEM channels thereby starting avalanche formation in them. Most of these secondary electrons will drift to the anode while the majority of ions is collected by the GEM electrodes. One GEM only can provide a gain of up to several thousand which is sufficient to detect minimum-ionising particles in the thin gaseous layer. By using two or three GEM detectors on top of each other, one can obtain a substantial total gain while a moderately low gain at each stage provides better stability and a higher discharge threshold [95, 98, 99].

7.5 Semiconductor track detectors

Basically, the *semiconductor track detector* is a set of semiconductor diodes described in Sect. 5.3. The main features of detectors of this family are discussed in various reviews [100–102].

The electrodes of the solid-state track detectors are segmented in the form of strips or pads. Figure 7.39 shows the operation principle of a silicon microstrip detector with sequential cathode readout [103].

A minimum-ionising particle crossing the depletion gap produces on average 90 electron–hole pairs per 1 μm of its path. For a typical detector of 300 μm thickness this resulted in a total collected charge well above the noise level of available electronics. The optimal pitch is determined by the carrier diffusion and by the spread of δ electrons which is typically 25 μm.

https://doi.org/10.1017/9781009401531.010 Published online by Cambridge University Press

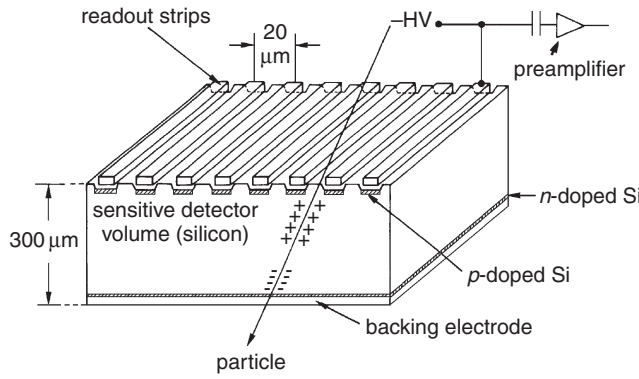

Fig. 7.39. Schematic layout of the construction of a silicon microstrip detector. Each readout strip is at negative potential. The strips are capacitively coupled (not to scale, from [103]).

The charge distribution on the readout strips allows a spatial resolution on the order of 10 µm or even better [104, 105]. To reduce the number of electronics channels only every second or third strip may be read out. Due to the large capacity between neighbouring strips, the so-called *floating strips* contribute to the centre-of-gravity value. Such silicon microstrip counters are frequently used in storage-ring experiments as vertex detectors, in particular, to determine the lifetimes of unstable hadrons in the picosecond range and to tag short-lived mesons in complicated final states. This technique of using silicon microstrip detectors in the vicinity of interaction points mimics the ability of high-resolution bubble chambers or nuclear emulsions (see Chap. 6) but uses a purely electronic readout. Because of the high spatial resolution of microstrip detectors, secondary vertices can be reconstructed and separated from the primary interaction relatively easily.

To measure the second coordinate, the n^+ side can also be divided into orthogonal strips. This encounters some technical difficulties which, however, can be overcome with a more complex structure [101, 102]. Readout electronics for microstrip detectors includes specifically developed chips bonded to the sensor plate. Each chip contains a set of preamplifiers and a circuit which sends signals to a digitiser using multiplexing techniques.

If a silicon chip is subdivided in a matrix-like fashion into many pads that are electronically shielded by potential wells with respect to one another, the energy depositions produced by complex events which are stored in the cathode pads can be read out pixel by pixel. The readout time is rather long because of the sequential data processing. It supplies, however, two-dimensional images in a plane perpendicular to the beam

direction. For a pixel size of $20 \times 20\,\mu m^2$ spatial resolutions of $5\,\mu m$ can be obtained. Because of the charge coupling of the pads, this type of silicon detector is also called a *charge-coupled device*. Commercially available *CCD detectors* with external dimensions of $1 \times 1\,cm^2$ have about 10^5 pixels [35, 106–108]. Modern devices in commercial cameras have up to 10 megapixels.

However, CCD detectors have some limitations. The depletion area is typically thin, 20–40 μm, which implies a rather small number of electron–hole pairs per minimum-ionising particle and, hence, requiring the necessity of CCD cooling to keep the dark current on an acceptable low level. Another drawback of CCDs is their slow data readout, a fraction of millisecond, that renders the use of this device at high-luminosity colliders difficult.

To avoid these limitations one has to return to the design as shown in Fig. 7.39 but with a segmentation of the p^+ side to pixels and connecting each pixel to individual preamplifiers. This technology has also been developed for the LHC experiments [109–111]. At present, the hybrid pixel technology is rather well established. Such a detector consists of the sensor and an integrated circuit board containing front-end electronics (Fig. 7.40). The connection of these two elements is made with the help of either solder (PbSn) or indium bump bonds.

Detectors of this type are being constructed now for LHC experiments [110, 111] as well as for X-ray counting systems [112, 113]. For medical imaging sensors with high-Z semiconductors, Cd(Zn)Te or GaAs, have also been made [114].

A pixel size of $\approx 50 \times 50\,\mu m^2$ is about the limit for hybrid pixel detectors. More promising is the technology of monolithic pixel detectors where both sensor and front-end electronics are integrated onto one silicon crystal. At present this technology is in the research and development stage [115, 116]. It is worth to mention that pixel detectors basically have a low capacity per pixel. According to Eq. (5.69) this results in low electronics noise.

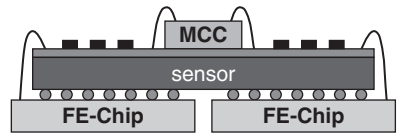

Fig. 7.40. An example of a hybrid pixel detector layout developed for the ATLAS detector [109]. The sensor plate containing pixels of $50\,\mu m \times 400\,\mu m$ is bonded to front-end (FE) chips via bump connection. The flex hybrid kapton layer atop the sensor carries additional electrical components and the module control chip (MCC).

https://doi.org/10.1017/9781009401531.010 Published online by Cambridge University Press

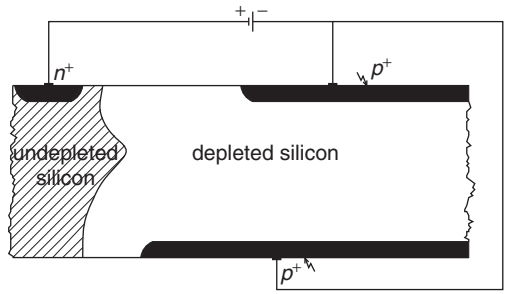

Fig. 7.41. Fabrication principle of a silicon drift chamber by sideward depletion [100, 119].

Silicon microstrip detectors can also operate as *solid-state drift chambers*. A review of this type of detectors can be found in [100, 117–119]. The working principle of a silicon drift chamber can be understood from Fig. 7.41.

The ohmic n^+ contact, normally extending over the whole surface of the detector, is now concentrated at one distinct position, which can be placed anywhere on the undepleted conducting bulk. Then diodes of p^+ layers can be put on both sides of the silicon wafer. At sufficiently high voltage between the n^+ contact and the p^+ layer the conductive bulk will be depleted and will retract into the vicinity of the n^+ electrode. In this way a potential valley is made in which electrons can move by, e.g. diffusion towards the n^+ readout contact. The produced holes will drift to the nearby p^+ contact.

If now an electric field with a field component parallel to the detector surface is added to such a structure, one arrives at a silicon drift chamber, where now the electrons produced by a photon or a charged particle in the depletion layer are guided by the drift field down the potential valley to the n^+ anode. Such a graded potential can be achieved by dividing the p^+ electrode into strips of suitably different potential (Fig. 7.42) [100, 119].

Silicon detectors will suffer radiation damage in a harsh radiation environment (see Chap. 12 on 'Ageing'). This presents a problem, in particular, at high-luminosity colliders where silicon detectors with excellent radiation hardness are required [100].

Silicon strip, pixel or voxel detectors are extremely useful in many different fields. Their small size, their high granularity, low intrinsic noise and the possibility to make them largely radiation resistant under special treatment render them a high-resolution detector of exceptional versatility. They are already now used at the heart of many particle physics experiments as vertex detectors or as focal-plane detectors in

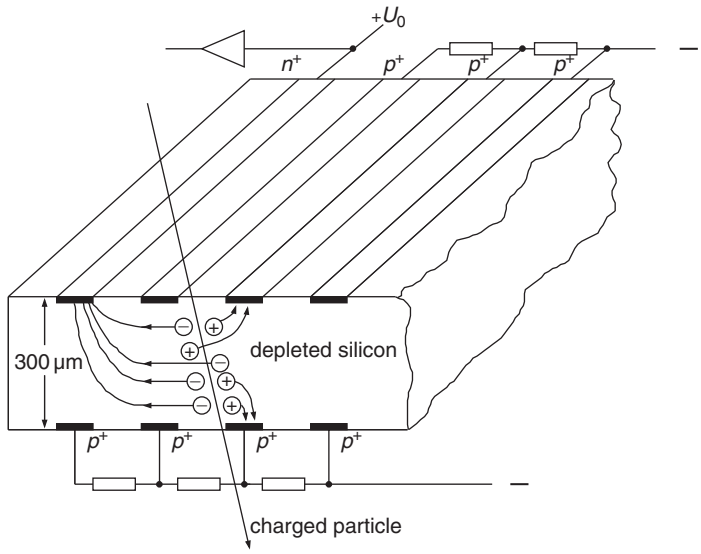

Fig. 7.42. Silicon drift chamber with graded potential [100, 117–119].

very successful satellite missions (Chandra, XMM Newton). Important applications in many other fields, like medicine (Compton cameras), art, material science and engineering (see Chap. 16) complete the large-scope applications.

7.6 Scintillating fibre trackers

A separate readout of individual *scintillating fibres* also provides an excellent spatial resolution which can even exceed the spatial resolution of drift chambers [120–122]. Similarly, thin capillaries (*macaronis*) filled with liquid scintillator can be used for tracking charged particles [123, 124]. In this respect, scintillating fibre calorimeters or, more generally, light-fibre systems can also be considered as tracking detectors. In addition, they represent, because of the short decay time of the scintillation flash, a genuine alternative to gas-discharge detectors, which are rather slow because of the intrinsically slow electron drift. Figure 7.43 shows the track of a charged particle in a stack of scintillating fibres. The fibre diameter in this case amounts to 1 mm [125].

Scintillating fibres, however, can also be produced with much smaller diameters. Figure 7.44 shows a microphotograph of a bundle consisting of scintillating fibres with 60 µm diameter. Only the central fibre is illuminated. A very small fraction of the light is scattered into the neighbouring fibres [126, 127]. The fibres are separated by a very thin

https://doi.org/10.1017/9781009401531.010 Published online by Cambridge University Press

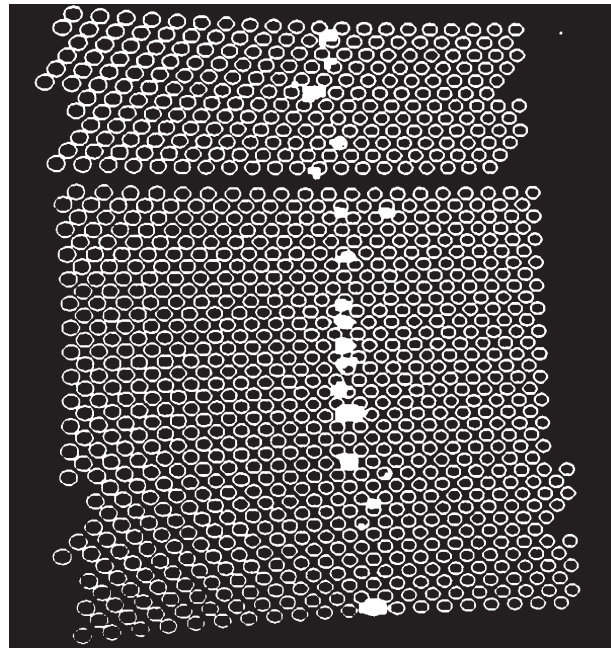

Fig. 7.43. Particle track in a stack of scintillating fibres; fibre diameter $\varnothing = 1\,\text{mm}$ [125].

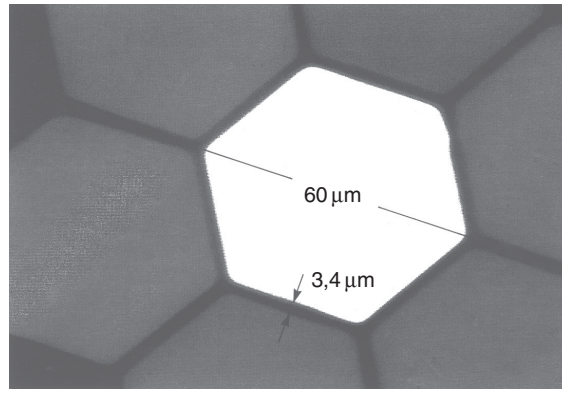

Fig. 7.44. Microphotograph of a bundle consisting of seven scintillating fibres. The fibres have a diameter of 60 µm. Only the central fibre is illuminated. The fibres are optically separated by a very thin cladding (3.4 µm) of lower refractive index to trap the light by total internal reflection. Only a small amount of light is scattered into the neighbouring fibres [126, 127].

https://doi.org/10.1017/9781009401531.010 Published online by Cambridge University Press

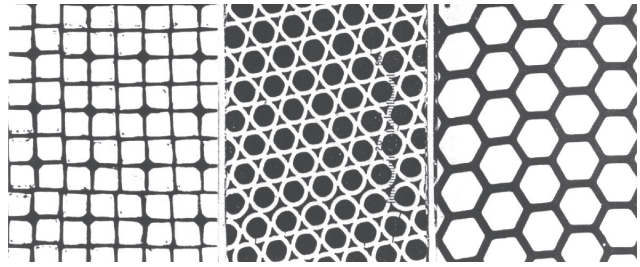

Fig. 7.45. Bundles of scintillating fibres from different companies (left: 20 µm; Schott (Mainz); centre: 20 µm; US Schott (Mainz); right: 30 µm plastic fibres; Kyowa Gas (Japan)) [129].

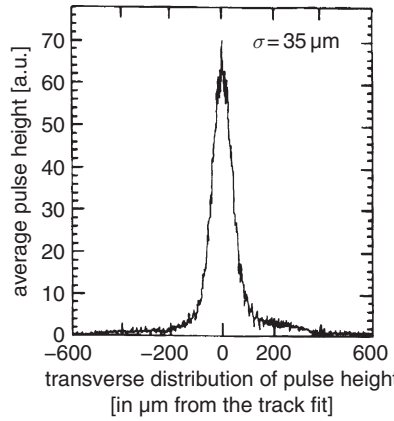

Fig. 7.46. Transverse pulse-height distribution of charged particles in a stack of 8000 scintillating fibres with 30 µm diameter [130].

cladding (3.4 µm). The optical readout system for such light-fibre systems, however, has to be made in such a way that the granular structure of the light fibres is resolved with sufficient accuracy, e.g. with optical pixel systems [128].

Arrangements of such fibre bundles are excellent candidates for tracking detectors in experiments with high particle rates requiring high time and spatial resolution. Figure 7.45 shows different patterns of bundles of scintillating fibres from different companies [129]. Figure 7.46 shows the spatial resolution for charged particles obtained in a stack consisting of 8000 scintillating fibres (30 µm diameter). A single-track resolution of 35 µm and a two-track resolution of 83 µm have been achieved [130].

https://doi.org/10.1017/9781009401531.010 Published online by Cambridge University Press

The transparency of scintillators can deteriorate in a high-radiation environment [131]. There exist, however, scintillator materials with a substantial radiation hardness [132, 133] (see also Chap. 12 on 'Ageing').

7.7 Problems

7.1 An unstable particle decays in the beam pipe of a storage-ring experiment into two charged particles which are measured in a three-layer drift chamber giving the drift times T_1^i, T_2^i, T_3^i ($T_1^1 = 300\,\text{ns}, T_2^1 = 195\,\text{ns}, T_3^1 = 100\,\text{ns}, T_1^2 = 400\,\text{ns}, T_2^2 = 295\,\text{ns}, T_3^2 = 200\,\text{ns}$). The two tracks make an angle of $\alpha = 60°$. Estimate the uncertainty with which the vertex of the two tracks can be reconstructed (drift velocity $v = 5\,\text{cm}/\mu\text{s}$). The resolution for all wires is assumed to be the same.

7.2 In a tracker with scintillating fibres ($\varnothing = 1\,\text{mm}$) one would like to instrument a volume of cross section $A = 20 \times 20\,\text{cm}^2$ as closely packed as possible. What is the maximum packing fraction that one can achieve with cylindrical fibres and how many does one need for the given cross-sectional area of the tracker?

7.3 The spatial resolution of a time-projection chamber is assumed to be $100\,\mu\text{m}$. In such a chamber the electric and magnetic fields are normally parallel. What kind of B field is required to keep the Larmor radii of the drifting electrons well below the spatial resolution (say, below $10\,\mu\text{m}$), if the maximum electron velocity perpendicular to B is $10\,\text{cm}/\mu\text{s}$?

7.4 60 keV X rays from a ^{241}Am source are to be measured in a proportional counter. The counter has a capacity of 180 pF. What kind of gas gain is required if the amplifier connected to the anode wire requires 10 mV at the input for a good signal-to-noise performance? The average energy to produce an electron–ion pair in the argon-filled counter is $W = 26\,\text{eV}$. What is the intrinsic energy resolution of the 60 keV line (the Fano factor for argon is $F = 0.17$)?

7.5 The wires in a multiwire proportional chamber (length $\ell = 1\,\text{m}$, diameter $30\,\mu\text{m}$, made of gold-plated tungsten) are strung with a weight of 50 g. Work out the sag of the wires under the influence of gravity!

The solution of this problem is normally given using variational methods [134–140]. Deviating from that solution the key assumption here is that the local horizontal and vertical forces in the wire define its local slope, where the wire itself is inelastic.

https://doi.org/10.1017/9781009401531.010 Published online by Cambridge University Press

References

[1] G. Charpak, *Electronic Imaging of Ionizing Radiation with Limited Avalanches in Gases*, Nobel-Lecture 1992, CERN-PPE-93-25 (1993); *Rev. Mod. Phys.* **65** (1993) 591–8

[2] G. Charpak *et al.*, The Use of Multiwire Proportional Chambers to Select and Localise Charged Particles, *Nucl. Instr. Meth.* **62** (1968) 202–68

[3] W. Bartl, G. Neuhofer, M. Regler & A. Taurok (eds.), Proc. 6th Int. Conf. on Wire Chambers, Vienna 1992, *Nucl. Instr. Meth.* **A323** (1992)

[4] G. Charpak *et al.*, Some Developments in the Operation of Multiwire Proportional Chambers, *Nucl. Instr. Meth.* **80** (1970) 13–34

[5] F. Sauli, *Principles of Operation of Multiwire Proportional and Drift Chambers*, CERN-77-09 (1977) and references therein

[6] G.A. Erskine, Electrostatic Problems in Multiwire Proportional Chambers, *Nucl. Instr. Meth.* **105** (1972) 565–72

[7] J. Va'vra, *Wire Chamber Gases*, SLAC-Pub-5793 (1992)

[8] J. Va'vra, Wire Chamber Gases, *Nucl. Instr. Meth.* **A323** (1992) 34–47

[9] Y.H. Chang, Gases for Drift Chambers in SSC/LHC Environments, *Nucl. Instr. Meth.* **A315** (1992) 14–20

[10] E.V. Anashkin *et al.*, Z-Chamber and Trigger of the CMD-2 Detector, *Nucl. Instr. Meth.* **A323** (1992) 178–83

[11] Particle Data Group, Review of Particle Physics, S. Eidelman *et al.*, *Phys. Lett.* **B592 Vol. 1–4** (2004) 1–1109; W.-M. Yao *et al.*, *J. Phys.* **G33** (2006) 1–1232; http://pdg.lbl.gov

[12] T. Trippe, *Minimum Tension Requirement for Charpak-Chamber Wires*, CERN NP Internal Report 69-18 (1969); P. Schilly *et al.*, Construction and Performance of Large Multiwire Proportional Chambers, *Nucl. Instr. Meth.* **91** (1971) 221–30

[13] M. Chew *et al.*, Gravitational Wire Sag in Non-Rigid Drift Chamber Structures, *Nucl. Instr. Meth.* **A323** (1992) 345–9

[14] H. Netz, *Formeln der Technik*, Hanser, München/Wien (1983)

[15] A.H. Walenta *et al.*, The Multiwire Drift Chamber: A New Type of Proportional Wire Chambers, *Nucl. Instr. Meth.* **92** (1971) 373–80

[16] A. Filatova *et al.*, Study of a Drift Chamber System for a K-e Scattering Experiment at the Fermi National Accelerator Lab., *Nucl. Instr. Meth.* **143** (1977) 17–35

[17] U. Becker *et al.*, A Comparison of Drift Chambers, *Nucl. Instr. Meth.* **128** (1975) 593–5

[18] M. Rahman *et al.*, A Multitrack Drift Chamber with 60 cm Drift Space, *Nucl. Instr. Meth.* **188** (1981) 159–63

[19] K. Mathis, *Test einer großflächigen Driftkammer*, Thesis, University of Siegen (1979)

[20] J. Allison, C.K. Bowdery & P.G. Rowe, *An Electrodeless Drift Chamber*, Int. Report, Univ. Manchester MC 81/33 (1981)

[21] J. Allison *et al.*, An Electrodeless Drift Chamber, *Nucl. Instr. Meth.* **201** (1982) 341–57

[22] Yu.A. Budagov *et al.*, How to Use Electrodeless Drift Chambers in Experiments at Accelerators, *Nucl. Instr. Meth.* **A255** (1987) 493–500
[23] A. Franz & C. Grupen, Characteristics of a Circular Electrodeless Drift Chamber, *Nucl. Instr. Meth.* **200** (1982) 331–4
[24] Ch. Becker *et al.*, Wireless Drift Tubes, Electrodeless Drift Chambers and Applications, *Nucl. Instr. Meth.* **200** (1982) 335–43
[25] G. Zech, Electrodeless Drift Chambers, *Nucl. Instr. Meth.* **217** (1983) 209–12
[26] R. Dörr, C. Grupen & A. Noll, Characteristics of a Multiwire Circular Electrodeless Drift Chamber, *Nucl. Instr. Meth.* **A238** (1985) 238–44
[27] A.H. Walenta & J. Paradiso, *The Time Expansion Chamber as High Precision Drift Chamber*, Proc. Int. Conf. on Instrumentation for Colliding Beam Physics; Stanford; SLAC-Report SLAC-R-250 UC-34d (1982) and SI-82-07 (1982) 1–29
[28] H. Anderhub *et al.*, Operating Experience with the Mark J Time Expansion Chamber, *Nucl. Instr. Meth.* **A265** (1988) 50–9
[29] E. Roderburg *et al.*, The Induction Drift Chamber, *Nucl. Instr. Meth.* **A252** (1986) 285–91
[30] A.H. Walenta *et al.*, Study of the Induction Drift Chamber as a High Rate Vertex Detector for the ZEUS Experiment, *Nucl. Instr. Meth.* **A265** (1988) 69–77
[31] E. Roderburg *et al.*, Measurement of the Spatial Resolution and Rate Capability of an Induction Drift Chamber, *Nucl. Instr. Meth.* **A323** (1992) 140–9
[32] D.C. Imrie, *Multiwire Proportional and Drift Chambers: From First Principles to Future Prospects*, Lecture delivered at the School for Young High Energy Physicists, Rutherford Lab. (September 1979)
[33] V.D. Peshekhonov, Wire Chambers for Muon Detectors on Supercolliders, *Nucl. Instr. Meth.* **A323** (1992) 12–21
[34] H. Faissner *et al.*, Modular Wall-less Drift Chambers for Muon Detection at LHC, *Nucl. Instr. Meth.* **A330** (1993) 76–82
[35] K. Kleinknecht, *Detektoren für Teilchenstrahlung*, Teubner, Stuttgart (1984, 1987, 1992); *Detectors for Particle Radiation*, Cambridge University Press, Cambridge (1986)
[36] S. Schmidt, private communication (1992)
[37] W.R. Kuhlmann *et al.*, Ortsempfindliche Zählrohre, *Nucl. Instr. Meth.* **40** (1966) 118–20
[38] H. Foeth, R. Hammarström & C. Rubbia, On the Localization of the Position of the Particle Along the Wire of a Multiwire Proportional Chamber, *Nucl. Instr. Meth.* **109** (1973) 521–4
[39] A. Breskin *et al.*, Two-Dimensional Drift Chambers, *Nucl. Instr. Meth.* **119** (1974) 1–8
[40] E.J. De Graaf *et al.*, Construction and Application of a Delay Line for Position Readout of Wire Chambers, *Nucl. Instr. Meth.* **166** (1979) 139–49
[41] L.G. Atencio *et al.*, Delay-Line Readout Drift Chamber, *Nucl. Instr. Meth.* **187** (1981) 381–6

[42] J.A. Jaros, *Drift and Proportional Tracking Chambers*, SLAC-Pub-2647 (1980)
[43] W. de Boer *et al.*, *Behaviour of Large Cylindrical Drift Chambers in a Superconducting Solenoid*, Proc. Wire Chamber Conf., Vienna (1980); *Nucl. Instr. Meth.* **176** (1980) 167–80
[44] PLUTO Collaboration, L. Criegee & G. Knies, e^+e^--Physics with the PLUTO Detector, *Phys. Rep.* **83** (1982) 151–280
[45] W.H. Toki, *Review of Straw Chambers*, SLAC-Pub-5232 (1990)
[46] V.M. Aulchenko *et al.*, Vertex Chamber for the KEDR Detector, *Nucl. Instr. Meth.* **A283** (1989) 528–31
[47] C. Biino *et al.*, A Very Light Proportional Chamber Constructed with Aluminised Mylar Tubes for Drift Time and Charge Division Readouts, *IEEE Trans. Nucl. Sci.* **36** (1989) 98–100
[48] G.D. Alekseev *et al.*, Operating Properties of Straw Tubes, *JINR-Rapid Communications*, No. 2 [41] (1990) 27–32
[49] V.N. Bychkov *et al.*, A High Precision Straw Tube Chamber with Cathode Readout, *Nucl. Instr. Meth.* **A325** (1993) 158–60
[50] F. Villa (ed.), *Vertex Detectors*, Plenum Press, New York (1988)
[51] D.H. Saxon, Multicell Drift Chambers, *Nucl. Instr. Meth.* **A265** (1988) 20–32
[52] E. Roderburg & S. Walsh, Mechanism of Wire Breaking Due to Sparks in Proportional or Drift Chambers, *Nucl. Instr. Meth.* **A333** (1993) 316–19
[53] J.A. Kadyk, J. Va'vra & J. Wise, Use of Straw Tubes in High Radiation Environments, *Nucl. Instr. Meth.* **A300** (1991) 511–17
[54] U.J. Becker *et al.*, Fast Gaseous Detectors in High Magnetic Fields, *Nucl. Instr. Meth.* **A335** (1993) 439–42
[55] R. Bouclier *et al.*, Fast Tracking Detector Using Multidrift Tubes, *Nucl. Instr. Meth.* **A265** (1988) 78–84
[56] Yu.P. Gouz *et al.*, Multi-Drift Module Simulation, *Nucl. Instr. Meth.* **A323** (1992) 315–21
[57] W. Bartel *et al.*, Total Cross-Section for Hadron Production by e^+e^- Annihilation at PETRA Energies, *Phys. Lett.* **B88** (1979) 171–7
[58] H. Drumm *et al.*, Experience with the JET-Chamber of the JADE Detector at PETRA, *Nucl. Instr. Meth.* **176** (1980) 333–4
[59] A. Wagner, Central Detectors, *Phys. Scripta* **23** (1981) 446–58
[60] O. Biebel *et al.*, *Performance of the OPAL Jet Chamber*, CERN-PPE-92-55 (1992); *Nucl. Instr. Meth.* **A323** (1992) 169–77
[61] F. Sauli, *Experimental Techniques*, CERN-EP-86-143 (1986)
[62] J. Bartelt, *The New Central Drift Chamber for the Mark II Detector at SLC*, Contribution to the 23rd Proc. Int. Conf. on High Energy Physics, Berkeley, Vol. 2 (1986) 1467–9
[63] D.R. Nygren, Future Prospects of the Time Projection Chamber Idea, *Phys. Scripta* **23** (1981) 584–96
[64] T. Lohse & W. Witzeling, The Time-Projection Chamber, in F. Sauli (ed.), *Instrumentation in High Energy Physics*, World Scientific, Singapore

(1992); The Time-Projection Chamber, *Adv. Ser. Direct. High Energy Phys.* **9** (1992) 81–155

[65] ALEPH Collaboration, D. Decamp *et al.*, ALEPH: A Detector for Electron–Positron Annihilations at LEP, *Nucl. Instr. Meth.* **A294** (1990) 121–78

[66] W.B. Atwood *et al.*, Performance of the ALEPH Time Projection Chamber, *Nucl. Instr. Meth.* **A306** (1991) 446–58

[67] Y. Sacquin, The DELPHI Time Projection Chamber, *Nucl. Instr. Meth.* **A323** (1992) 209–12

[68] C. Rubbia, *The Liquid Argon Time Projection Chamber: A New Concept for Neutrino Detectors*, CERN-EP-77-08 (1977)

[69] P. Benetti *et al.*, *The ICARUS Liquid Argon Time Projection Chamber: A New Detector for ν_τ-Search*, CERN-PPE-92-004 (1992)

[70] A. Bettini *et al.*, The ICARUS Liquid Argon TPC: A Complete Imaging Device for Particle Physics, *Nucl. Instr. Meth.* **A315** (1992) 223–8

[71] F. Pietropaolo *et al.*, *The ICARUS Liquid Argon Time Projection Chamber: A Full Imaging Device for Low Energy e^+e^- Colliders?*, Frascati INFN-LNF 91-036 (R) (1991)

[72] G. Buehler, *The Liquid Argon Time Projection Chamber*, Proc. Opportunities for Neutrino Physics at BNL, Brookhaven (1987) 161–8

[73] J. Seguinot *et al.*, Liquid Xenon Ionization and Scintillation: Studies for a Totally Active-Vector Electromagnetic Calorimeter, *Nucl. Instr. Meth.* **A323** (1992) 583–600

[74] P. Benetti *et al.*, *A Three Ton Liquid Argon Time Projection Chamber*, INFN-Report DFPD 93/EP/05, University of Padua (1993); *Nucl. Instr. Meth.* **A332** (1993) 395–412

[75] C. Rubbia, *The Renaissance of Experimental Neutrino Physics*, CERN-PPE-93-08 (1993)

[76] G. Carugno *et al.*, A Self Triggered Liquid Xenon Time Projection Chamber, *Nucl. Instr. Meth.* **A311** (1992) 628–34

[77] E. Aprile *et al.*, Test of a Two-Dimensional Liquid Xenon Time Projection Chamber, *Nucl. Instr. Meth.* **A316** (1992) 29–37

[78] A. Oed, Position Sensitive Detector with Microstrip Anode for Electron Multiplication with Gases, *Nucl. Instr. Meth.* **A263** (1988) 351–9

[79] P.M. McIntyre *et al.*, Gas Microstrip Chambers, *Nucl. Instr. Meth.* **A315** (1992) 170–6

[80] F. Sauli, *New Developments in Gaseous Detectors*, CERN-EP-2000-108 (2000)

[81] L. Shekhtman, Micro-pattern Gaseous Detectors, *Nucl. Instr. Meth.* **A494** (2002) 128–41

[82] M. Hoch, Trends and New Developments in Gaseous Detectors, *Nucl. Instr. Meth.* **A535** (2004) 1–15

[83] F. Angelini *et al.*, *A Microstrip Gas Chamber with True Two-dimensional and Pixel Readout*, INFN-PI/AE 92/01 (1992); *Nucl. Instr. Meth.* **A323** (1992) 229–35

[84] F. Angelini, A Thin, Large Area Microstrip Gas Chamber with Strip and Pad Readout, *Nucl. Instr. Meth.* **A336** (1993) 106–15
[85] F. Angelini *et al.*, *A Microstrip Gas Chamber on a Silicon Substrate*, INFN, Pisa PI/AE 91/10 (1991); *Nucl. Instr. Meth.* **A314** (1992) 450–4
[86] F. Angelini *et al.*, *Results from the First Use of Microstrip Gas Chambers in a High Energy Physics Experiment*, CERN-PPE-91-122 (1991)
[87] J. Schmitz, *The Micro Trench Gas Counter: A Novel Approach to High Luminosity Tracking in HEP*, NIKHEF-H/91-14 (1991)
[88] R. Bouclier *et al.*, *Microstrip Gas Chambers on Thin Plastic Supports*, CERN-PPE-91-227 (1991)
[89] R. Bouclier *et al.*, *Development of Microstrip Gas Chambers on Thin Plastic Supports*, CERN-PPE-91-108 (1991)
[90] R. Bouclier *et al.*, *High Flux Operation of Microstrip Gas Chambers on Glass and Plastic Supports*, CERN-PPE-92-53 (1992)
[91] F. van den Berg *et al.*, Study of Inclined Particle Tracks in Micro Strip Gas Counters, *Nucl. Instr. Meth.* **A349** (1994) 438–46
[92] B. Schmidt, Microstrip Gas Chambers: Recent Developments, Radiation Damage and Long-Term Behavior, *Nucl. Instr. Meth.* **A419** (1998) 230–8
[93] Y. Giomataris *et al.*, MICROMEGAS: A High-Granularity Position-Sensitive Gaseous Detector for High Particle-Flux Environments, *Nucl. Instr. Meth.* **A376** (1996) 29–35
[94] F. Sauli, GEM: A New Concept for Electron Amplification in Gas Detectors, *Nucl. Instr. Meth.* **A386** (1997) 531–4
[95] F. Sauli, Progress with the Gas Electron Multiplier, *Nucl. Instr. Meth.* **A522** (2004) 93–8 (Most recent review)
[96] B. Peyaud *et al.*, KABES: A Novel Beam Spectrometer for NA48, *Nucl. Instr. Meth.* **A535** (2004) 247–52
[97] D. Thers *et al.*, Micromegas as a Large Microstrip Detector for the COMPASS Experiment, *Nucl. Instr. Meth.* **A469** (2001) 133–46
[98] A. Buzulutskov, A. Breskin, R. Chechik *et al.*, The GEM Photomultiplier Operated with Noble Gas Mixtures, *Nucl. Instr. Meth.* **A443** (2000) 164–80. (Triple-GEM introduction. High-gain operation of the triple-GEM in pure noble gases and their mixtures. GEM-based photomultiplier with CsI photocathode.)
[99] A. Bondar, A. Buzulutskov, A. Grebenuk, *et al.* Two-Phase Argon and Xenon Avalanche Detectors Based on Gas Electron Multipliers, *Nucl. Instr. Meth.* **A556** (2006) 273–80 (GEM operation at cryogenic temperatures, including in the two-phase mode)
[100] G. Lutz, *Semiconductor Radiation Detectors*, Springer, Berlin (1999)
[101] H. Dijkstra & J. Libby, Overview of Silicon Detectors, *Nucl. Instr. Meth.* **A494** (2002) 86–93
[102] M. Turala, Silicon Tracking Detectors – Historical Overview, *Nucl. Instr. Meth.* **A541** (2005) 1–14
[103] R. Horisberger, *Solid State Detectors*, Lectures given at the III ICFA School on Instrumentation in Elementary Particles Physics, Rio de Janeiro, July 1990, and PSI-PR-91-38 (1991)

[104] J. Straver *et al.*, *One Micron Spatial Resolution with Silicon Strip Detectors* CERN-PPE-94-26 (1994)

[105] R. Turchetta, Spatial Resolution of Silicon Microstrip Detectors, *Nucl. Instr. Meth.* **A335** (1993) 44–58

[106] P.N. Burrows, A CCD Vertex Detector for a High-Energy Linear e^+e^- Collider, *Nucl. Instr. Meth.* **A447** (2000) 194–201

[107] M. Cargnelli *et al.*, Performance of CCD X-ray Detectors in Exotic Atom Experiments, *Nucl. Instr. Meth.* **A535** (2004) 389–93

[108] M. Kuster *et al.*, *PN-CCDs in a Low-Background Environment: Detector Background of the Cast X-Ray Telescope*, Conference on UV, X-ray and Gamma-ray Space Instrumentation for Astronomy, San Diego, California, 1–3 August 2005, e-Print Archive: physics/0508064

[109] N. Wermes, Pixel Detector for Particle Physics and Imaging Applications, *Nucl. Instr. Meth.* **A512** (2003) 277–88

[110] W. Erdmann, The CMS Pixel Detector, *Nucl. Instr. Meth.* **A447** (2000) 178–83

[111] F. Antinori, A Pixel Detector System for ALICE, *Nucl. Instr. Meth.* **A395** (1997) 404–9

[112] S.R. Amendolia *et al.*, Spectroscopic and Imaging Capabilities of a Pixellated Photon Counting System, *Nucl. Instr. Meth.* **A466** (2001) 74–8

[113] P. Fischer *et al.*, A Counting Pixel Readout Chip for Imaging Applications, *Nucl. Instr. Meth.* **A405** (1998) 53–9

[114] M. Lindner *et al.*, Comparison of Hybrid Pixel Detectors with Si and GaAs Sensors, *Nucl. Instr. Meth.* **A466** (2001) 63–73

[115] P. Holl *et al.*, Active Pixel Matrix for X-ray Satellite Mission, *IEEE Trans. Nucl. Sci.* **NS-47**, No. 4 (2000) 1421–5

[116] P. Klein *et al.*, A DEPFET Pixel Bioscope for the Use in Autoradiography, *Nucl. Instr. Meth.* **A454** (2000) 152–7

[117] E. Gatti *et al.* (ed.), Proc. Sixth European Symp. on Semiconductor Detectors, New Developments in Radiation Detectors, *Nucl. Instr. Meth.* **A326** (1993)

[118] E. Gatti & P. Rehak, Semiconductor Drift Chamber – An Application of a Novel Charge Transport Scheme, *Nucl. Instr. Meth.* **A225** (1984) 608–14

[119] L. Strüder, High-Resolution Imaging X-ray Spectrometers, in H.J. Besch, C. Grupen, N. Pavel, A.H. Walenta (eds.), *Proceedings of the 1st International Symposium on Applications of Particle Detectors in Medicine, Biology and Astrophysics, SAMBA '99* (1999) 73–113

[120] A. Simon, *Scintillating Fiber Detectors in Particle Physics*, CERN-PPE-92-095 (1992)

[121] M. Adinolfi *et al.*, *Application of a Scintillating Fiber Detector for the Study of Short-Lived Particles*, CERN-PPE-91-66 (1991); *Nucl. Instr. Meth.* **A310** (1991) 485–9

[122] D. Autiero *et al.*, Study of a Possible Scintillating Fiber Tracker at the LHC and Tests of Scintillating Fibers, *Nucl. Instr. Meth.* **A336** (1993) 521–32

[123] J. Bähr *et al.*, *Liquid Scintillator Filled Capillary Arrays for Particle Tracking*, CERN-PPE-91-46 (1991); *Nucl. Instr. Meth.* **A306** (1991) 169–76
[124] N.I. Bozhko *et al.*, *A Tracking Detector Based on Capillaries Filled with Liquid Scintillator*, Serpukhov Inst., High Energy Phys. 91-045 (1991); *Nucl. Instr. Meth.* **A317** (1992) 97–100
[125] *CERN: Tracking by Fibers*, CERN-Courier, **27(5)** (1987) 9–11
[126] *Working with High Collision Rates*, CERN-Courier, **29(10)** (1989) 9–11
[127] C. D'Ambrosio *et al.*, Reflection Losses in Polystyrene Fibers, *Nucl. Instr. Meth.* **A306** (1991) 549–56; private communication by C. D'Ambrosio (1994)
[128] M. Salomon, New Measurements of Scintillating Fibers Coupled to Multianode Photomultipliers, *IEEE Trans. Nucl. Sci.* **39** (1992) 671–3
[129] *Scintillating Fibers*, CERN-Courier, **30(8)** (1990) 23–5
[130] D. Acosta *et al.*, Advances in Technology for High Energy Subnuclear Physics. Contribution of the LAA Project, *Riv. del Nuovo Cim.* **13 (10–11)** (1990) 1–228; G. Anzivino *et al.*, The LAA Project, *Riv. del Nuovo Cim.* **13(5)** (1990) 1–131
[131] G. Marini *et al.*, *Radiation Damage to Organic Scintillation Materials*, CERN-85-08 (1985)
[132] J. Proudfoot, *Conference Summary: Radiation tolerant Scintillators and Detectors*, Argonne Nat. Lab. ANL-HEP-CP-92-046 (1992)
[133] G.I. Britvich *et al.*, Investigation of Radiation Resistance of Polystyrene-Based Scintillators, *Instr. Exp. Techn.* **36** (1993) 74–80
[134] J.J. O'Connor & E.F. Robertson, Catenary, www-gap.dcs.st-and.ac.uk/~history/Curves/Catenary.html (1997)
[135] Catenary: http://mathworld.wolfram.com/Catenary.html (2003)
[136] The Schiller Institute, Two Papers on the Catenary Curve and Logarithmic Curve (Acta Eruditorium, 1691, G.W. Leibniz, translated by Pierre Beaudry), www.schillerinstitute.org/fid_97-01/011_catenary.html (2001)
[137] Hanging chain www.math.udel.edu/MECLAB/UndergraduateResearch/Chain/Main_Page.html
[138] Th. Peters, *Die Kettenlinie*, www.mathe-seiten.de (2004)
[139] http://mathsrv.ku-eichstaett.de/MGF/homes/grothmann/Projekte/Kettenlinie/
[140] Die Mathe-Redaktion, *Die Kettenlinie als Minimalproblem*, http://matheplanet.com/default3.html?article=506 (2003)